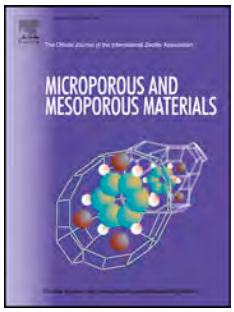

Effect of red mud added to zeolite LTA synthesis: Where is Fe in the newly-formed material?

Claudia Belviso, Carla Cannas, Nicola Pinna, Francesco Cavalcante, Antonio Lettino, Paolo Lotti, G. Diego Gatta

PII: S1387-1811(20)30061-5

DOI: https://doi.org/10.1016/j.micromeso.2020.110058

Reference: MICMAT 110058

To appear in: *Microporous and Mesoporous Materials*

Received Date: 16 September 2019

Revised Date: 28 November 2019

Accepted Date: 29 January 2020

Please cite this article as: C. Belviso, C. Cannas, N. Pinna, F. Cavalcante, A. Lettino, P. Lotti, G.D. Gatta, Effect of red mud added to zeolite LTA synthesis: Where is Fe in the newly-formed material?, *Microporous and Mesoporous Materials*, https://doi.org/10.1016/j.micromeso.2020.110058.

Effect of red mud added to zeolite LTA synthesis: Where is Fe in the newly-formed material?

Claudia Belviso[1*], Carla Cannas[2], Nicola Pinna[3], Francesco Cavalcante[1], Antonio Lettino[1], Paolo Lotti[4], G. Diego Gatta[4*]

[1]Istituto di Metodologie per l'Analisi Ambientale – CNR, Tito Scalo (PZ), 85050, Italy

[2]Dipartimento di Scienze Chimiche e Geologiche and INSTM, Università di Cagliari, Complesso Universitario di Monserrato, Monserrato, CA, Italy

[3]Humboldt-Universität zu Berlin, Institut für Chemie, Berlin, 12489, Germany

[4]Dipartimento di Scienze della Terra, Università degli Studi di Milano, Milan, 20133, Italy

Corresponding authors:

Claudia Belviso - IMAA–CNR, Tito Scalo (Potenza), Italy. claudia.belviso@imaa.cnr.it - phone:+390971427224; fax:+390971427222

G. Diego Gatta - Università degli Studi di Milano (Milan), Italy. diego.gatta@unimi.it

ABSTRACT

In this work, silica and alumina pure sources were used to perform the synthesis of zeolite A (LTA) by both conventional and pre-fused hydrothermal processes. Increasing amount of red mud (RM, a waste formed during the caustic leaching of bauxite to produce alumina and rich in Fe) was added during the synthesis processes. We attempted to investigate if the use of pure sources with the addition of different amounts of red mud promotes, or hinder, the crystallization of the zeolite A and if Fe is structurally-incorporated into the newly-formed zeolite structure (*i.e.*, as framework or extra-framework cation) or if it is concentrated in a proper Fe-rich phase. The results carried out using a multi-methodological approach (laboratory X-ray powder diffraction; synchrotron radiation powder X-ray diffraction; scanning electron microscopy and electron transmission microscopy coupled with EDX elemental mapping) show that LTA zeolite crystals (with cubic morphology) can be efficiently formed using pure source combined with variable amount of red mud. The use of complementary analytical techniques indicate that Fe coming from the red mud is not structurally-incorporated into the newly-formed zeolite crystals, but it is mainly concentrated in nano-clusters of Fe-oxides (with spinel-type structure) located on the zeolite crystal surface. The utilization of non-conventional Fe source, here represented by red mud, can be considered as the first step toward a new solidification/stabilization process for this waste, as dictated by the regenerative economy route. These data make an important contribution to understanding the role played by surface phenomena on zeolite crystals when transition elements are used in the synthesis procedure.

Keywords: LTA; zeolite surface; red mud; waste; Fe-bearing nanoparticles

1. Introduction

LTA-type zeolite is a synthetic zeolite which empirical formula is $[Me_x][Al_{12}Si_{12}O_{48}]$, where *Me* represent the metal cations [1]. Its structure consists of simple β-cages, which are composed of 24

tetrahedra. The links of the β-cages is provided through double four-membered rings of tetrahedra. The interconnection of these units produces a large cavity (the so-called α-cage), ~11.4 Å in diameter, and two intersecting channel systems.

Due to the Si:Al molar ratio close to 1, LTA is a low-silica zeolite easily synthesized from kaolinite characterized by the same atomic Si/Al atomic ratio [2-8]. However, beside this common natural source, processes based on the utilization of pure aluminate and silicate suspensions [9-14] or different waste materials [15-24] have been largely used to direct the crystallization of this type of zeolite.

Literature data have documented the synthesis of magnetic or Fe-modified LTA zeolite [25-27]. However, studies on Fe-zeolites are currently orientated to consider iron as structurally-incorporated framework/extra-framework component [26, 28-33], although there are several open questions about the incorporation mechanisms of trivalent cations into the structure of zeolites. A very few studies in the open literature reported evidence that in Fe-modified zeolites most of the iron is not concentrated as extra-framework cation, but it is rather deposited on the surface of crystals in the form of nano-aggregates of Fe-oxides [34,35].

One of the low-cost source of Fe is the so-called “red mud” (RM). It is, in fact, the waste material produced by the caustic leaching process used to extract aluminium from bauxite, considered an important source of this element. The name ‘red mud’ comes from its red colour due to the abundant presence of iron, mainly as oxy-hydroxides. However, the composition of this waste varies according to the differences in the refining processes as well as to the mineralogical nature of the bauxite ores [36-40].The increasing alumina request worldwide has led to an increase in RM production. Power and co-workers [41] estimated at 120 million tonnes the annual world production rate of red mud, taking into account that about 1.5 t of RM is discharged for every ton of produced alumina. During the period from the late 19th century to 2008, more than 2.7 billion tonnes of red mud were generated [42]; in 2011, the annual production of RM in China was 42.6 million t and it reached 73 million t in 2013 [43,44]. The huge production of this waste causes serious pollution

problems. The high pH, as well as the chemical composition characterized by the presence of heavy metals and radioactive elements, generates environmental problems when large volume of this waste material has to be disposed. The main methods used in the past (prior to the 1970s) for RM disposal were marine discharge and lagooning [41]. These methods were replaced by a new RM disposal concept represented by a "dry" stacking in bonded area line with different kind of barrier materials [45]. However, in the recent years, much effort has been made to recycle red mud, in the framework of circular economy design processes. The key to solve environmental problems caused by RM is, in fact, to develop technologies able to convert this waste into a secondary resource [43] such as, *e.g.*, bricks, concrete admixtures, and road base materials [46-48]. Many studies have also showed different processes for the recovery of major metals (*e.g.*, Fe, Al and Ti) [49,50] or minor metals (e.g., rare earth elements) [51] from RM. In our previous papers, red mud was used as alumina source to form zeolite [52] or as complementary material to synthesize zeolite with magnetic property, without the addition of external magnetic nanoparticles[17]. However, in those studies, Fe speciation in the newly-formed magnetic zeolite was not analysed, leaving open questions about the actual location of Fe: lying into the structure of the newly-formed zeolite or in a proper Fe-rich species?.

In this study, we investigated the effect of red mud addition to the IZA synthesis protocol of LTA in order to describe, on the basis of a multi-methodological approach (laboratory X-ray powder diffraction-XRPD; synchrotron radiation powder X-ray diffraction-SR/XRD; scanning electron microscopy –SEM and electron transmission microscopy-TEM coupled with EDX elemental mapping), if 1) the use of pure sources with the addition of different amounts of red mud promotes, or not, the crystallization of the zeolite A, by both conventional and pre-fused hydrothermal processes and 2) if Fe is structurally-incorporated into the zeolite structure (*i.e.*, as framework or extra-framework cation) or concentrated in a different Fe-bearing phase, . These experimental findings are also preparatory for a potential solidification/stabilization process for the red mud waste, following the route inspired to the regenerative economy.

2. Experimental section

2.1. Materials

The reactant used during the synthesis were pure sodium hydroxide pellets, sodium aluminate, sodium silicate and deionised water for the preparation of the initial precursor suspension. Variable amount of red mud from aluminium extraction area of Sulcis, Cagliari (Italy) was also added. All chemicals of reagent grade were purchased from Aldrich Chemicals Ltd.

2.2. Zeolite Synthesis

Conventional hydrothermal synthesis. 80 mL of distilled water with 0.723 g of sodium hydroxide were gently mixed until NaOH was completely dissolved. Half of this solution was added to 8.3 g of sodium aluminate and mixed until clear to prepare Solution A.

Solution B was prepared by dissolving 15.48 g of sodium silicate in the second half of NaOH solution previously prepared. Then solution A was quickly added into solution B under vigorous stirring. The resulted suspension was continuously stirred for 1 night, and then subjected to treatment at 40 °C for 4 days. The solid fraction was finally extracted via centrifugation followed by drying in an oven at 80 °C. The process was repeated adding 4, 8 and 12 g of red mud sample to the Solution A, in different experiments. The samples were labelled as S3, S5 and S6, respectively.

Pre-fused hydrothermal synthesis. Solution A was prepared by dissolving NaOH, pre-fused red mud (at 600 °C) and 8.3 g of sodium aluminate in 40 mL distilled water. Solution B was prepared as described above. Solution A was quickly added into solution B, stirred for 1 nigh and treated at 40 °C for 4 days. The solids was separated by centrifugation and dried as described above to recover the solid fraction for further characterizations. Also for the pre-fused hydrothermal synthesis, the process was repeated preparing Solution A with the addition of 4, 8 and 12 g of pre-fused red mud, in different experiments. The new samples were labelled as S9, S10 and S11, respectively.

The samples synthesised without red mud addition were labelled as pure LTA and used as reference.

2.3. Characterization

Scanning Electron Microscopy (SEM). Crystal size and habit of the synthetic products were investigated using a Zeiss Supra 40 scanning electron microscope with Field Emission Gun (SEM-FEG), equipped with an energy dispersive spectrometer (EDS). The samples were carbon-sputtered (10 nm thick) in order to avoid charging of the surface.

Laboratory X-ray powder diffraction (XRPD). Preliminary information on the crystalline phases formed by both conventional and pre-fused hydrothermal processes were obtained by X-ray diffraction from polycrystalline samples using a Rigaku Rint Miniflex powder diffractometer, equipped with Cu-*K*α radiation. The XRD patterns were collected in Bragg–Brentano geometry in the angular range 3°–70° of 2θ, step-size of 0.02°, scan-step time of 3 s, accelerating voltage of 30 kV and electric current at the Cu anode of 15 mA.

Synchrotron radiation X-ray diffraction (SR-XRD). SR-XRD experiments were carried out at the MCX beamline (2) [53] of the ELETTRA-Sincrotrone Trieste S.C.p.A. facility (Basovizza, Trieste, Italy). Samples were loaded into borosilicate glass capillaries with 300 μm diameter. The diffraction patterns were collected in transmitting geometry, with capillary kept spinning during the data collection. An incident X-ray beam of 12 keV in energy was used. Full-profile fits were performed by the Rietveld method, using the GSAS package (http://www.ccp14.ac.uk/solution/gsas/). The structure refinement protocol is described in Gatta and co-authors [54].

Trasmission Electron Microscopy (TEM). The samples for transmission electron microscopy were prepared by drop-coating a carbon coated copper TEM grid with a dispersion of the material in ethanol. TEM observations have been carried out on a field emission gun FEI TALOS F200S at an

acceleration voltage of 200 kV. The microscope is equipped with an integrated EDS system with two silicon drift detectors, for qualitative and semi-quantitative chemical analysis.

Elemental analysis. The chemical composition of red mud sample was determined by X-ray fluorescence (XRF), with a Philips PW 1480 instrument. Elemental analyses were also performed with an energy-dispersive X-ray spectrometer (EDS, Oxford Inca Energy 350) equipped with a Si(Li) detector.

3. Results and discussion

The chemical composition of the red mud displays the presence of large fraction of FeO (37.04 %), along with Zn (6.76 %) and Pb (3.61 %), thus indicating that it is a potentially toxic waste. SiO_2 and Al_2O_3 are scarce and the fraction of these oxides is 4.23% and 0.89 %, respectively (Table 1). The chemical data are confirmed by the XRPD investigation (Fig. 1): the diffraction patterns show the presence of natrojarosite [ideally $NaFe_3(SO_4)_2(OH)_6$], Pb-natrojarosite [ideally $PbFe_6(SO_4)4(OH)_{12}$], franklinite [ideally $ZnFe_2O_4$] and gunningite [ideally $ZnSO_4 \cdot H_2O$]. Conventional XRPD and SR-XRD measurements indicate that the uses of pure sources with the addition of different amounts of red mud promotes the crystallization of the zeolite A, by both conventional and pre-fused hydrothermal process. LTA without the addition of RM (*i.e.*, pure LTA, $Na_{12}Al_{12}Si_{12}O_{48}$) was also synthesized and taken as a reference material. XRPD patterns are shown in Fig. 2. The diffraction patterns display a generally decrease in peaks intensity with the increase in red mud content. Beside zeolite LTA, franklinite and hematite are detected as well on X-ray profiles after conventional (samples S3, S5 and S6) (Fig. 2a) and pre-fused hydrothermal process (samples S9, S10, S11) (Fig. 2b), respectively. However, weak diffraction peaks suggest the presence of a low fraction of franklinite also in the S10 sample. The weight fraction (wt%) of the different phases was determined by Rietveld full-profile fit on the SR-XRD patterns [55]. The data indicate that the amount of LTA formed by conventional hydrothermal method ranges from ~91wt% in S5 to ~98wt % in S3. S6 displays ~93 wt% of the newly-formed zeolite (Table 2). The fraction of franklinite

detected in the same samples is ~2 wt% in S3, ~9 wt% in S5 and ~7 wt% in S6 (Table 2). The quantitative analysis carried out on the samples formed by pre-fused hydrothermal process indicate that a lower amount of LTA is formed (~83wt%). The results also show the presence of about 16wt% of hematite (Table 2).

Based on the aforementioned results, it is possible to consider that natrojarosite and Pb-natrojarosite (characterizing the red mud composition) were dissolved during hydrothermal process, thus making Fe and Pb available to be involved in the zeolite crystallization process. The presence of franklinite in conventional hydrothermal products (Fig. 2a) indicates that this phase was only partially involved into dissolution process. The pre-fusion treatment, instead, was more effective in franklinite dissolution, making larger amount of Fe available to form hematite as precipitated phase (Fig. 2b). However, no linear correlation is observed between the weight fraction of zeolite and the amount of red mud added during both the synthesis processes.

Scanning electron microscopy provided information on the habit of the crystallites formed by both conventional and pre-fused hydrothermal methods. Pure LTA is shown in Fig. S1. Although the typical cubic shape of this type of zeolite, SEM images display cubes with rather rounded faces and edges. The size of the crystallites ranges from 20-30 nm to 1 μm. A well-defined cubic habit instead characterizes all the samples formed with the addition of red mud. In detail, Fig. S2 shows LTA synthesised by hydrothermal process with 4 g (S3), 8 g (S5) and 12 g (S6) of RM, respectively, whereas Fig. S3 displays the zeolites formed by pre-fused hydrothermal method with the same amount of red mud: *i.e.*, 4 g for S9, 8 g for S10 and 12 g S11. It is interesting to point out that increasing the content of red mud, the cubic habit is better defined, as shown by crystals with faces and edges very well outlined. Moreover, SEM data also indicate that the pre-fused process generally improve the zeolite synthesis.

The presence of Fe associated with the newly-formed zeolite is documented by EDX analysis. Fig. 3 shows a representative spectrum of the investigated samples. However, the SEM-EDX investigation cannot provide a unique answer about the presence of Fe as structurally-incorporated

element (*i.e.*, as framework or extra-framework component) or in the form of nanoparticles precipitated on the crystallites surface, as observed by Kragović and co-workers [35]. In order to confirm or deny the presence of Fe as structurally-incorporated element, Rietveld structure refinements were performed on the basis of SR-XRD data of the synthesis products. A careful inspection was first of all devoted to the intra-tetrahedral (T-O) bond distances, to detect the potential substitution of Si or Al with Fe^{3+}. The results indicate that the T-O bond distances are always consistent with the expected values of Si or Al as tetrahedral cations (Table S1), ruling out a significant presence of Fe as framework component. The potential presence of Fe as extra-framework cation was also investigated, by careful inspection of the difference-Fourier maps of the electron density function. However, the residuals of the electron density maps do not provide unequivocal evidence of the presence of Fe into the zeolitic cavities.

The aforementioned experimental findings based on X-ray diffraction data show that it is not possible to confirm or deny the presence of structurally-incorporated Fe into the newly-formed zeolite. On this basis, and considering the previous experiments reported by Kragović et al. [35], a TEM investigation of the synthesis products was performed. TEM data of both LTA synthesised by hydrothermal process (S3, S5 and S6) (Fig. S4) and pre-fused hydrothermal method (S9, S10 and S11) (Fig. S5) show idiomorphic crystals of zeolite with nano-aggregates on their surfaces. In order to further analyse the potential distribution of metal cations in zeolite crystals and in the nano-aggregates lying on the crystals surfaces, EDX elemental mapping was performed for Si, Al, Fe, Zn and Pb on samples formed by both conventional and pre-fused hydrothermal process (Figs. 4-6). The EDX maps carried out on S5 sample clearly show that Si and Al are well distributed (and perfectly overlapping) (Fig. 4a, b) in the crystals of the LTA zeolite, and almost absent in the nano-clusters. EDX- maps show instead a different distribution of Zn and Fe (Fig. 4c, d) that, however, is superimposable between these two elements but not with Si and Al. These data indicate that the transition metal cations are not incorporated in the Si-Al-bearing structure of the synthetic zeolite, but they form irregular aggregates of nano-sized particles. This is particularly evident in the case of

Fe (Fig. 4d). This behaviour is also confirmed by the EDX maps in Figure 10, showing well-defined zeolite crystals primarily with additional Fe and Zn-bearing nanoparticles (Fig. 5b and c).This figure also displays Pb elemental dispersion (Fig. 5b) comparable with the other metal cations. EDX maps carried out on the S10 sample (synthesised by pre-fused hydrothermal method) confirmed the same experimental findings already described for the S5 sample (Fig. 6). Furthermore, the electron diffraction patterns (Fig. 7 and 8) prove that the Fe-Zn-bearing nano-clusters lying on the surface of the zeolite crystallites are mainly constituted by Fe-Zn-spinels (franklinite $ZnFe_2O_4$ with magnetite-like structure).

Chemical (by elemental maps) and structure (electron diffraction patterns) evidence are, therefore, mutually consistent, and corroborates the previous experimental findings reported by Kragović and co-workers [35], who investigated the behaviour of iron in Fe-modified zeolite formed using $FeCl_2$ solution. In the experiments of our study, instead, we investigated the behaviour of iron from the red mud in relation to the newly formed LTA zeolite. To complete the investigation on the role played by surface phenomena on zeolite crystals in presence of iron, additional experiments were also performed to synthesise zeolite with Fe in the form of nano-magnetite by conventional hydrothermal method (SnM). Also in this case, TEM results display the formation of idiomorphic crystals of zeolite with nano-aggregates on the surfaces (Fig. 9). EDX elemental mapping (Fig. 10) indicates that Si and Al are perfectly overlapping in the crystals of the LTA zeolite, and almost absent in the nano-clusters that instead are characterized by Fe and O composition. These data indicate that nano-magnetite does not dissolve during hydrothermal process but it precipitates on the surface of the newly-formed zeolite.

Based on the new results discussed in this manuscript, and according with some previously published literature data [35,53], it is possible to infer that transition metals, such as Fe or Zn, tend to form nano-clusters on the crystal surfaces of zeolite instead of being incorporated as framework/extra-framework component, as many studies on Fe-zeolites are still orientated to consider.

4. Conclusions

The results reported in this paper show that LTA zeolite can be efficiently formed using pure source combined with variable amount of a waste material: red mud. The use of complementary analytical techniques indicate thatthe Fe coming from the red mud is not structurally-incorporated into the newly-formed zeolite crystals, but it is mainly concentrated in nano-clusters of Fe-oxides (with spinel-type structure) located on the zeolite crystal surface. This behaviour is also shared by the other metal cations of this system: Zn and Pb.

These data make an important contribution to understanding the role played by surface phenomena on zeolite crystals when transition elements are used in the synthesis procedure. Moreover, the utilization of 'non-conventional Fe source', here represented by red mud, can be considered the first step toward a new solidification/stabilization process for this waste, as dictated by the regenerative economy route. However, before any potential utilization of this protocol on an industrial scale, a deep investigation on mobility of Fe/Zn/Pb nano-clusters precipitated on the newly-formed zeolite needs to be performed by chemical sequential extraction process, and this will be the aim of a future investigation.

Aknowledgments

This work was supported by RAS – Regione Autonoma della Sardegna CESA - Piano Sulcis (E58C16000080003). ELETTRA-Sincrotrone Trieste S.C.p.A. (Basovizza, Trieste, Italy) is acknowledged for the allocation of beamtime. Christoph Erdmann is acknowledged for measuring HRTEM and S/TEM. Three anonymous reviewers are thanked for their suggestions aimed to improve the quality of the manuscript.

References

[1] V. Gramlich, W.M. Z. Meier, The crystal structure of hydrated NaA: a detailed refinement of a pseudosymmetric zeolite structure, Z. Kristallogr. 133 (1971) 134–149.

[2] C. Belviso, F Cavalcante, A. Lettino, S. Fiore, A and X type zeolite synthesized from kaolinite at low temperature, Appl. Clay Sci. 80-81 (2013) 162-168.

[3] A. Gualtieri, M. Bellotto, Modelling the structure of the metastable phases in the reaction sequence kaolinite-mullite by X-ray scattering experiments, Phys. Chem. Miner. 25 (1998) 442–452.

[4] A. Gualtieri, P. Norby, G. Artioli, J. Hanson, Kinetics of formation of zeolite Na-A [LTA] from natural kaolinites, Phys. Chem. Miner. 24 (1997) 191–199.

[5] D. Massiot, P. Dion, J.F. Alcover, F. Bergaya, ^{27}Al and ^{29}Si MAS NMR study of kaolinite thermal decomposition by controlled rate thermal analysis, J. Am. Ceram. Soc. 11 (1995) 2940–2944.

[6] C.A. Ríos, C.D. Williams, M.A. Fullen, Nucleation and growth history of zeolite LTA synthesized from kaolinite by two differentmethods, Appl. Clay Sci. 42 (2009) 446–454.

[7] S. Chandrasekhar, Influence of metakaolinization temperature on the formation of zeolite 4A from kaolin, Clay Min. 31 (1996) 253–261.

[8] L. Heller-Kallai, I. Lapides, Reactions of kaolinites and metakaolinites with NaOH-comparison of different samples (part 1), Appl. Clay Sci. 35 (2007) 99–107.

[9] L.V.C. Rees, S. Chandrasekhar, Formation of zeolite from the system Na_2O–Al_2O_3–SiO_2–H_2O in alkaline medium (pH>10), Zeolites 13 (1993) 524–533.

[10] S. Mintova, N.H. Olson, V. Valtchev, T. Bein, Nanocrystal growth from colloids at room temperature, Science 28 (1999) 958-960.

[11] P.S. Singh, V.K. Aswal, S.G. Chaudhri, W. Schwieger, Structural evolution during nucleation of Si-rich LTA nanocrystals from colloidal solution, Microporous Mesoporous Mat. 259 (2018) 99-110.

[12] D.O. Matthew, J.A. Soltis, T.C. Marlon, R. Lee Penn, J.D. Rimer, Nucleation of FAU and LTA Zeolites from Heterogeneous Aluminosilicate Precursors, Chem. Mater. 28 (2016) 4906−4916.

[13] T.F. Chaves, F.L.F. Soares, D. Cardoso, R.L. Carneiro, Monitoring of the crystallization of zeolite LTA using Raman and chemometric tools, Analyst 140 (2015) 854–859.

[14] R. Grizzetti, Artioli G., Kinetics of nucleation and growth of zeolite LTA from clear solution by in situ and ex situ XRPD, Microporous Mesoporous Mat. 54 (2002) 105-112.

[15] H.L. Chang W.H. Shih, Synthesis of zeolites A and X from fly ashes and their ion-exchange with cobalt ions, Ind. Eng. Chem. Res. 39 (2000) 4185-4191.

[16] Belviso C., Ultrasonic vs hydrothermal method: different approaches to convert fly ash into zeolite. How they affect the stability of synthetic products over time?, Ultrason. Sonochem. 43 (2018) 9-14

[17] C. Belviso, E. Agostinelli, S. Belviso, F. Cavalcante, S. Pascucci,. D. Peddis, G. Varvaro, Fiore S. Synthesis of magnetic zeolite at low temperature using a waste material mixture: fly ash and red mud, Microporous Mesoporous Mat. 202 (2015) 208-216.

[18] C. Belviso, L.G. Giannossa, F.J. Huertas, A. Lettino, A. Mangone, S. Fiore, Synthesis of zeolites at low temperatures in fly ash-kaolinite mixtures, Microporous Mesoporous Mat. 212 (2015) 35-47.

[19] Y. Li, T. Peng, W. Man, L. Ju, F. Zheng, M. Zhang, Guo M., Hydrothermal synthesis of mixtures of NaA zeolite and sodalite from Ti-bearing electric arc furnace slag, RSC Adv. 6 (2016) 8358–8366.

[20] T. Qian, J. Li, Synthesis of Na-A zeolite from coal gangue with the in-situ crystallization technique, Adv. Powder Technol. 26 (2015) 98–104.

[21] N.R.C.F. Machado, D.M.M. Miotto, Synthesis of Na-A and -X zeolites from oil shale ash, Fuel 84 (2005) 2289–2294.

[22] S.Yamazaki, K. Tsutsumi, Conventional hydrothermal synthesis of Na-A zeolite from

cupola slag and aluminum sludge, Microporous Mesoporous Mat 37 (2000) 67–80.

[23] V. Psycharis, V. Perdikatsis, G. Christidis, Crystal structure and Rietveld refinement of zeolite A synthesized from fine-grained perlite waste materials, Bull. Geol. Soc. Greece 36 (2004) 121-129.

[24] F. Collins, A. Rozhkovskaya, J. G. Outram, G. J. Millar, A critical review of waste resources, synthesis, and applications for Zeolite LTA. Microporous Mesoporous Mat 291, 2020, 109667.

[25] B. Divband, M. R. Rashidi, M. Khatamian, G. R. Kazemi Eslamian, N. Gharehaghaji, F. Dabaghi Tabriz, Linde Type A and nano magnetite/NaA zeolites: cytotoxicity and doxorubicin loading efficiency, Open Chem. 16 (2018) 21-28.

[26] K. Lázár, C. Vincent, P. Fejes, Variety of available coordination sites for extra-framework iron in LTA and MFI zeolites, Hyperfine Interact 187 (2008) 1-6.

[27] P. Fejes, I. Kiricsi, K. Kovács, K. Lázár, I. Marsi, A. Oszkó, A. Rockenbauer, Z. Schay, Incorporation of iron in sodalite structures and their transformation into other iron containing zeolites synthesis of Fe-NaA (LTA), Appl. Catal. A-Gen. 223 (2002) 147-160.

[28] M. Petrera, A. Gennaro, P. Gherardi, G. Gubitosa, N. Pernicon, Mossbauer Study of Iron-containing Zeolites, J. Chem. SOC., Faraday Trans. I 80 (1984) 709-720.

[29] R. Kumar, P. Ratnasamy, Isomorphous substitution of iron in the framework of zeolite ZSM-23, J. Catal. 121 (1990) 86-98.

[30] P. Fejes, J.B. Nagy, K. Lázár, J. Halász, Heat-treatment of isomorphously substituted ZSM-5 (MFI) zeolites An ESR and Mössbauer spectroscopy and kinetic study, Appl. Catal. A-Gen. 190 (2000) 117-135.

[31] M.M. Emara, A.S.M. Tourky, M.M. El-Moselhy, Structural modification of mordenite zeolite with Fe for the photo-degradation of EDTA, J. Hazard. Mater. 166 (2009) 514-522.

[32] G.Li, E.A. Pidko, R.A. van Santen, C. Li, E.J.M. Hensen, Stability of Extraframework Iron-Containing Complexes in ZSM-5 Zeolite, J. Phys. Chem. C. 117 (2013) 413-426.

[33] N. Senamart, S. Buttha, W. Pantupho, I.Z. Koleva, S. Loiha, H.A. Aleksandrov, J. Wittayakun, G.N. Vayssilov, Characterization and temperature evolution of iron-containing species in HZSM-5 zeolite prepared from different iron sources, J. Porous Mat. 26 (2019) 1227-1240.

[34] M.J. Jiménez-Cedillo, M.T. Olguín, Ch. Fall, A. Colín, Adsorption capacity of iron–or iron–manganese-modified zeolite-rich tuffs for As(III) and As(V) water pollutants, Appl. Clay Sci. 54 (2011) 206–216.

[35] M. Kragović, A. Daković, M. Marković́a, J. Krstić, G.D. Gatta, N. Rotiroti, Characterization of lead sorption by the natural and Fe(III)-modified zeolite, Appl. Surf. Sci. 283 (2013) 764– 77.

[36] Y. Liu, C. Lin, Y. Wu, Characterization of red mud derived from a combined Bayer Process and bauxite calcination method, J. Hazard. Mater. 146 (2007) 255-261.

[37] P. Smith, The processing of high silica bauxites — Review of existing and potential processes, Hydrometallurgy 98 (2009) 162-176.

[38] M. Gräfe, G. Power, C. Klauber, Bauxite residue issues: III. Alkalinity and associated chemistry, Hydrometallurgy 108 (2011) 60-79.

[39] C. Hanahan, D. McConchie, J. Pohl, R. Creelman, M. Clark and C. Stocksiek, Chemistry of seawater neutralization of bauxite refinery residues (red mud), Environ. Eng. Sci. 21 (2004) 125-138.

[40] L. Santona, P. Castaldi, P. Melis, Evaluation of the interaction mechanisms between red muds and heavy metals, J. Hazard. Mater. 136 (2006) 324-329.

[41] G. Power, M. Gräfe, C. Klauber, Bauxite residue issues: I. Current management, disposal and storage practices, Hydrometallurgy 108 (2013) 33-45.

[42] C. Si, Y. Ma, C. Lin, Red Mud as a Carbon Sink: Variability, Affecting Factors and Environmental Significance, J Hazard Mater 15 (2012) 244-245.

[43] L. Wang, N. Sun, H. Tang, W. Sun, A Review on Comprehensive Utilization of Red Mud and Prospect Analysis, Minerals 9 (2019) 362-380.

386 [44] Y. Hua, K.V. Heal, W. Frieslhanl, The use of red mud as an immobiliser for metal/metalloid-
387 contaminated soil: A review, J. Hazard. Mater. 325 (2017) 17–30.
388 [45] C. Belviso, S. Pascucci, Red mud: Abrief review on conventional and unconventional
389 techniques used to characterize this wastematerial. In:" Red Mud: Production, Composition and
390 Impact". Nova Science Publishers, Inc., 2018, 1-30.
391 [46] S. Liu, X. Guan, S. Zhang, C. Xu, H. Li, J. Zhang, Sintering red mud based imitative ceramic
392 bricks with CO_2 emissions below zero, Mater. Lett. 191 (2017) 222–224.
393 [47] E. Ujaczki, Y. Zimmermann, C. Gasser, M. Molnár, V. Feigl, M. Lenz, Red mud as secondary
394 source for critical raw materials–extraction study, J. Chem. Technol. Biotechnol. 92 (2017) 2835–
395 2844.
396 [48] Q. Guan, W. Sun, Y. Hu, Z. Yin, C. Zhang, C. Guan, X. Zhu, S. Ahmed Khoso, Simultaneous
397 control of particle size and morphology of α-CaSO4 · 1/2H2O with organic additives, J. Am. Ceram.
398 Soc. 102 (2019) 2440–2450.
399 [49] B. Mishra, A. Staley, D. Kirkpatrick, Recovery of value-added products from red mud, Miner.
400 Metall. Process 19 (2002) 87–94.
401 [50] R. Paramguru, P. Rath, V. Misra, Trends in red mud utilization - a review, Miner. Process.
402 Extract. Metall. Rev. 26 (2005) 1–29.
403 [51] C. Klauber, M. Gräfe, G. Power, Bauxite residue issues: II. Options for residue utilization,
404 Hydrometallurgy 108 (2011) 11-32.
405 [52] C. Belviso, A. Kharchenko, E. Agostinelli, F. Cavalcante, D. Peddis, G. Varvaro, N. Yaacoube,
406 S. Mintova, Red mud as aluminium source for the synthesis of magnetic zeolite, Microporous
407 Mesoporous Mat. 270 (2018) 24–29.
408 [53] J.R. Plaisier, L. Nodari, L. Gigli, E.P. Rebollo San Miguel, R. Bertoncello, A. Lausi,
409 The X-ray diffraction beamline MCX at Elettra: a case study of non-destructive analysis on stained
410 glass, Acta Imeko 6 (2017) 71-75.

411 [54] G.D. Gatta, P. Cappelletti, B. de' Gennaro, N. Rotiroti, A.Langella, New data on Cu-
412 exchanged phillipsite: a multi-methodological study, Phys. Chem. Minerals 42 (2015) 723-733.
413 [55] A. Altomare, C. Cuocci, G.D. Gatta, A.Moliterni, R. Rizzi, Methods of crystallography:
414 powder X-ray diffraction. EMU Notes in Mineralogy, 2017, 19, Chapter 2, 79–138.

415
416
417
418
419
420
421
422
423
424
425
426
427
428
429
430

Captions

Figure 1.
XRPD patterns of the red mud used in this study.

Figure 2.
XRPD profiles of synthesis products by: [a] conventional hydrothermal process [b] pre-fused hydrothermal process

Figure 3.
EDX spectrum representative of the LTA zeolite crystals formed by adding RM during the synthesis

Figure 4.
TEM images (left-up) and relative EDX elemental mapping of : *a*) Si, *b*) Al, *c*) Zn and *d*) Fe. S5 sample.

Figure 5.
TEM images (left-up) and EDX elemental mapping of : *a*) Si, *b*) Al, *c*) Zn, *d*) Fe and *e*) Pb. S5 sample.

Figure 6.
TEM images (left-up) and EDX elemental mapping of Si, Al, Zn, Fe and Pb elements (*a*-*e*). S10 sample.

Figure 7.
S5 sample. *a*) high-resolution image of a zeolite crystal and irregular aggregates of nano-sized particles lying on its surface; *b*) electron diffraction pattern showing single spots ascribable to the zeolite crystal and diffraction rings generated by the Fe-Zn-bearing nano-clusters (highly likely with spinel-type structure). A table with the geometric parameters is provided.

Figure 8.
S10 sample. *a*) high-resolution images of zeolite crystals and irregular aggregates of nano-sized particles; *b*) co-existing electron diffraction patterns of a zeolite crystal and Fe-Zn bearing nano-clusters (with a table of their geometric parameters).

Figure 9.
TEM images of the SnM zeolite formed by conventional hydrothermal synthesis with nano-magnetite.

Figure 10.
TEM images (left-up) and EDX elemental mapping of : *a*) Si, *b*) Al, *c*) O and *d*) Fe. SnM sample.

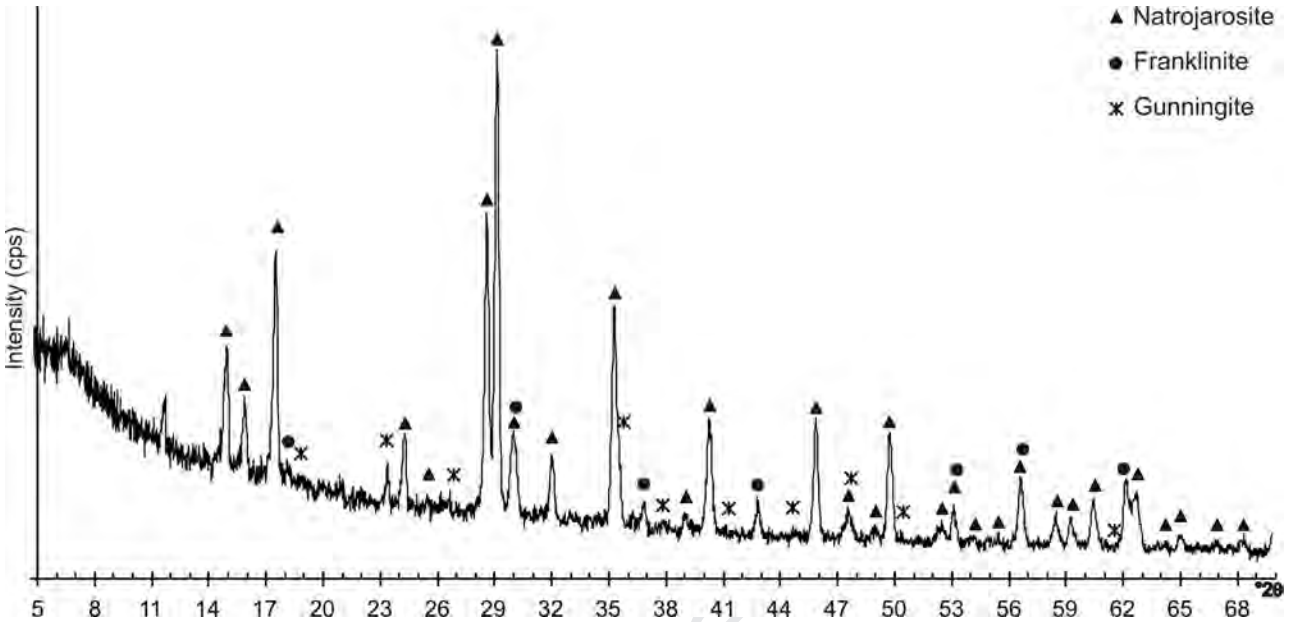

Figure 1

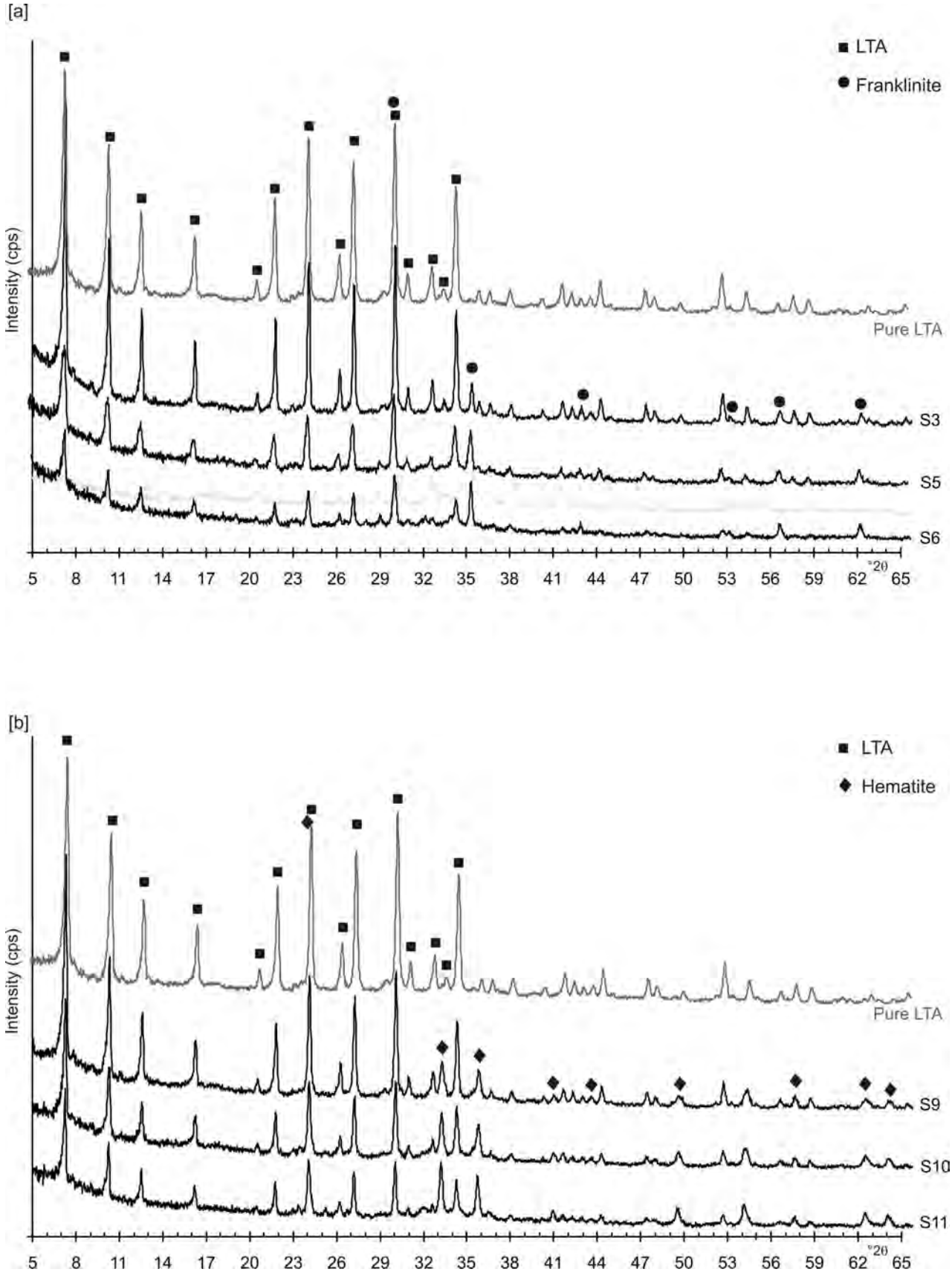
[a]
LTA
Franklinite
Intensity (cps)
Pure LTA
S3
S5
S6
5 8 11 14 17 20 23 26 29 32 35 38 41 44 47 50 53 56 59 62 65
°2θ
[b]
LTA
Hematite
Intensity (cps)
Pure LTA
S9
S10
S11
5 8 11 14 17 20 23 26 29 32 35 38 41 44 47 50 53 56 59 62 65
°2θ

Figure 2

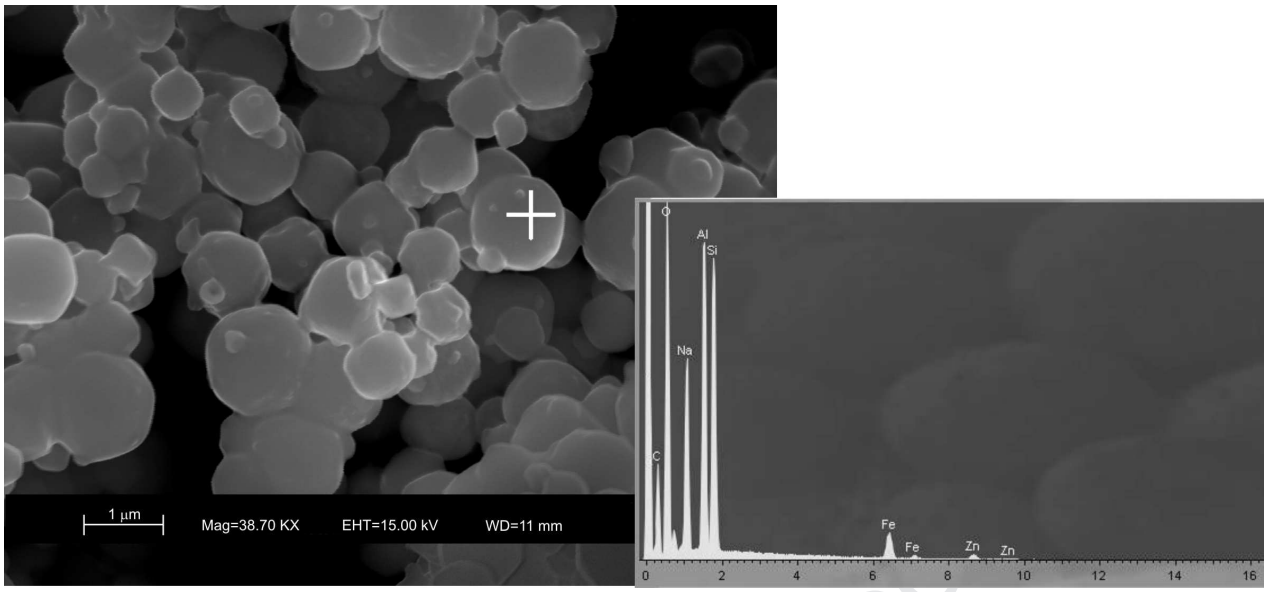

Figure 3

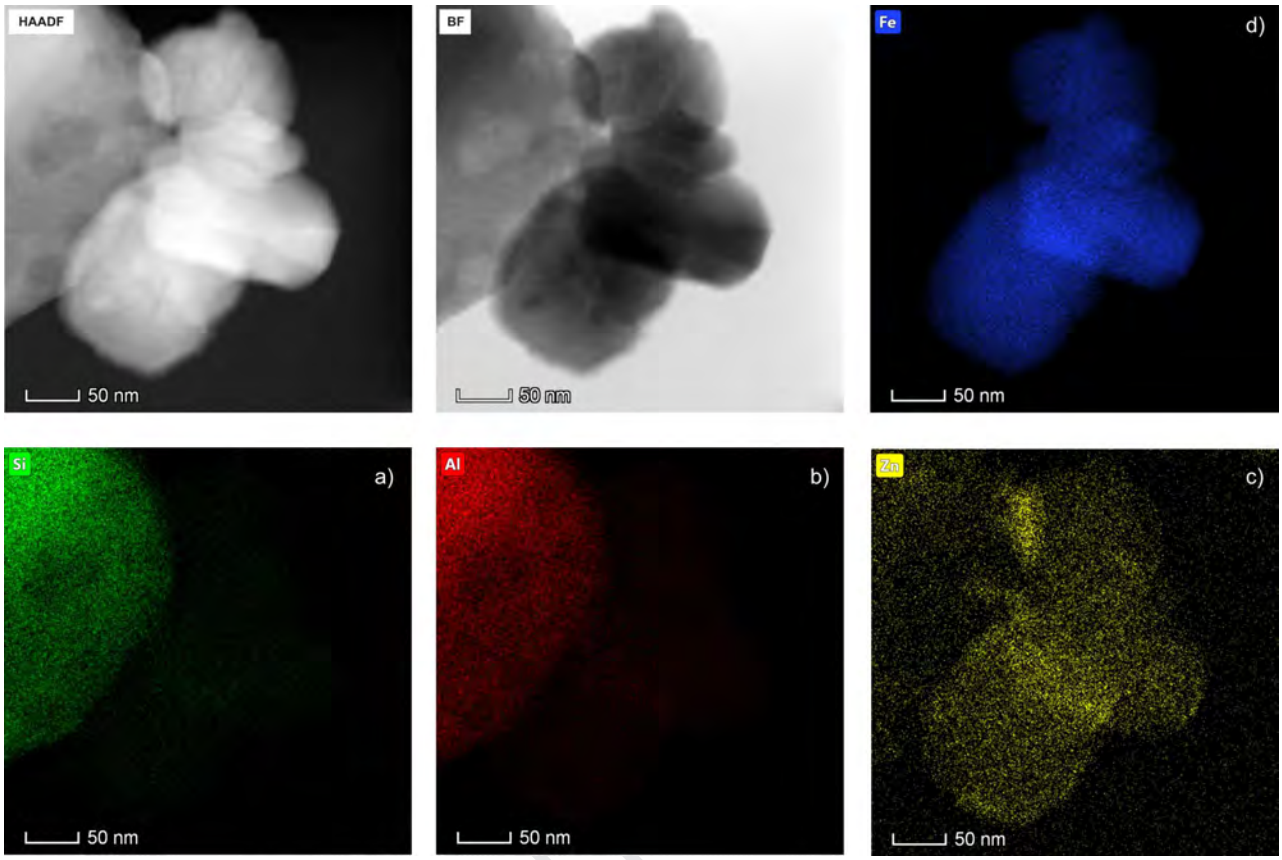

Figure 4

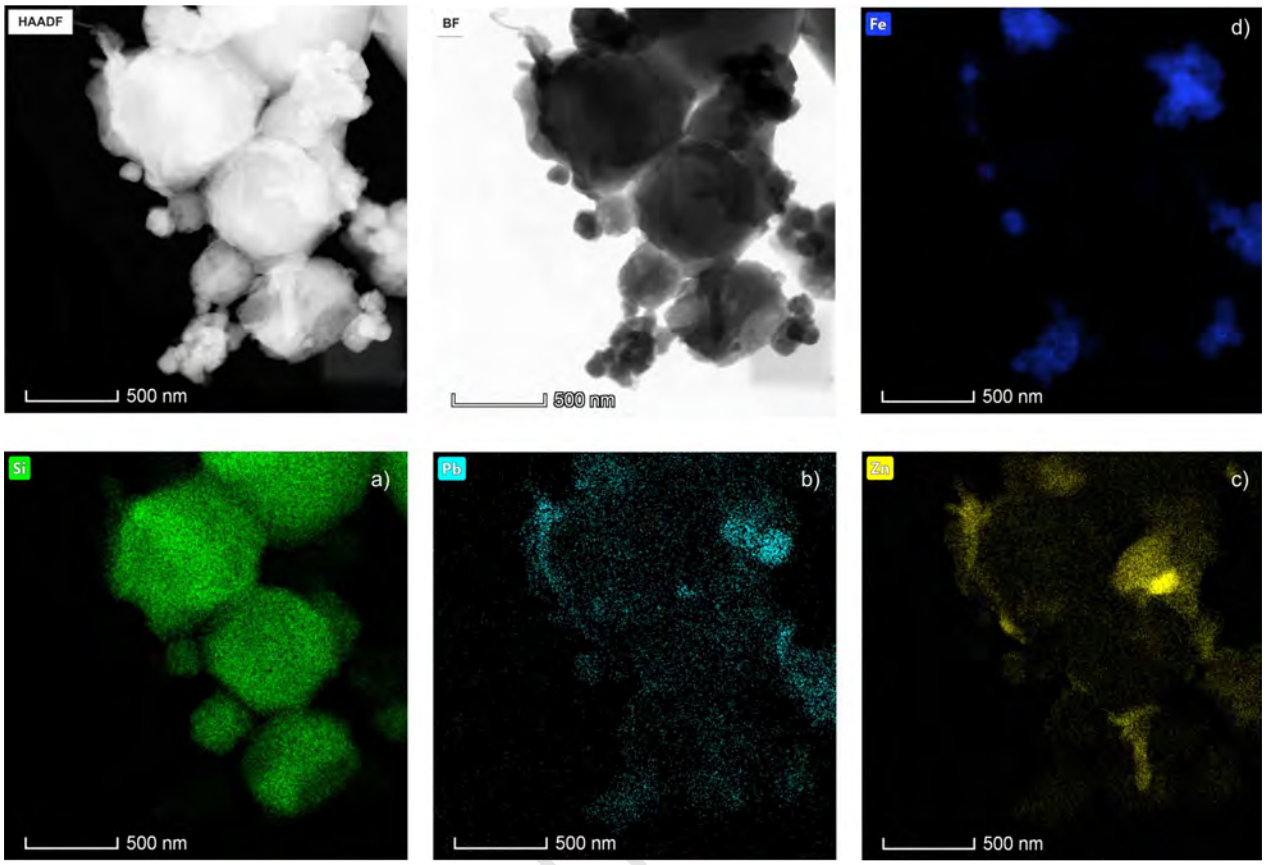

Figure 5

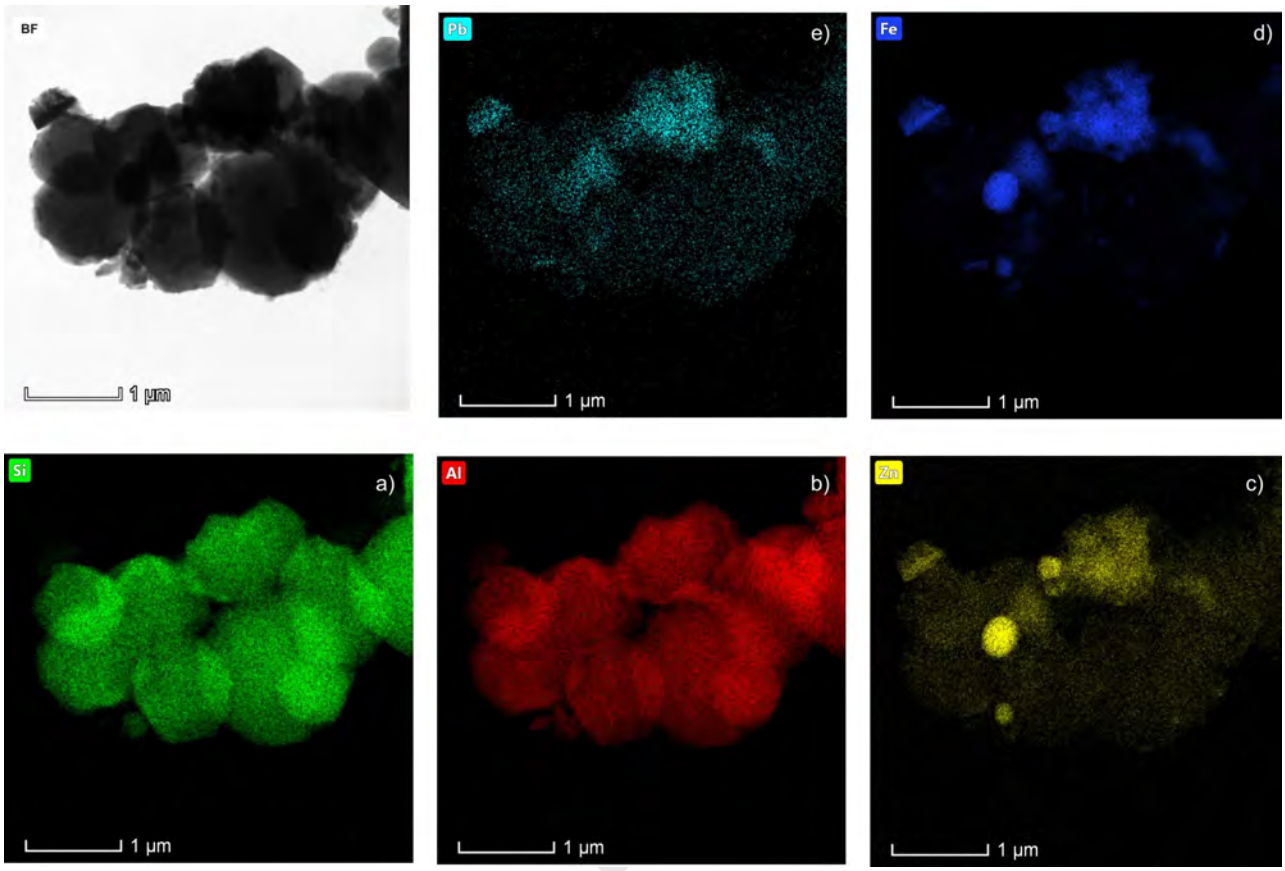

Figure 6

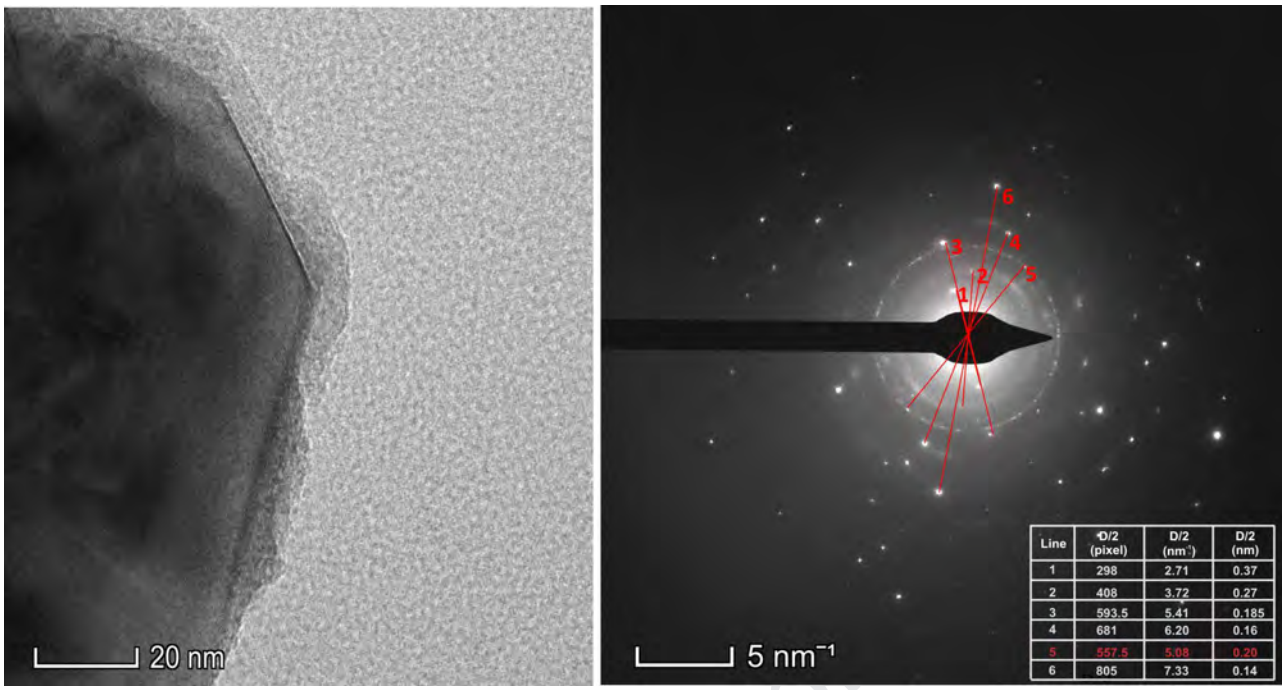

Figure 7

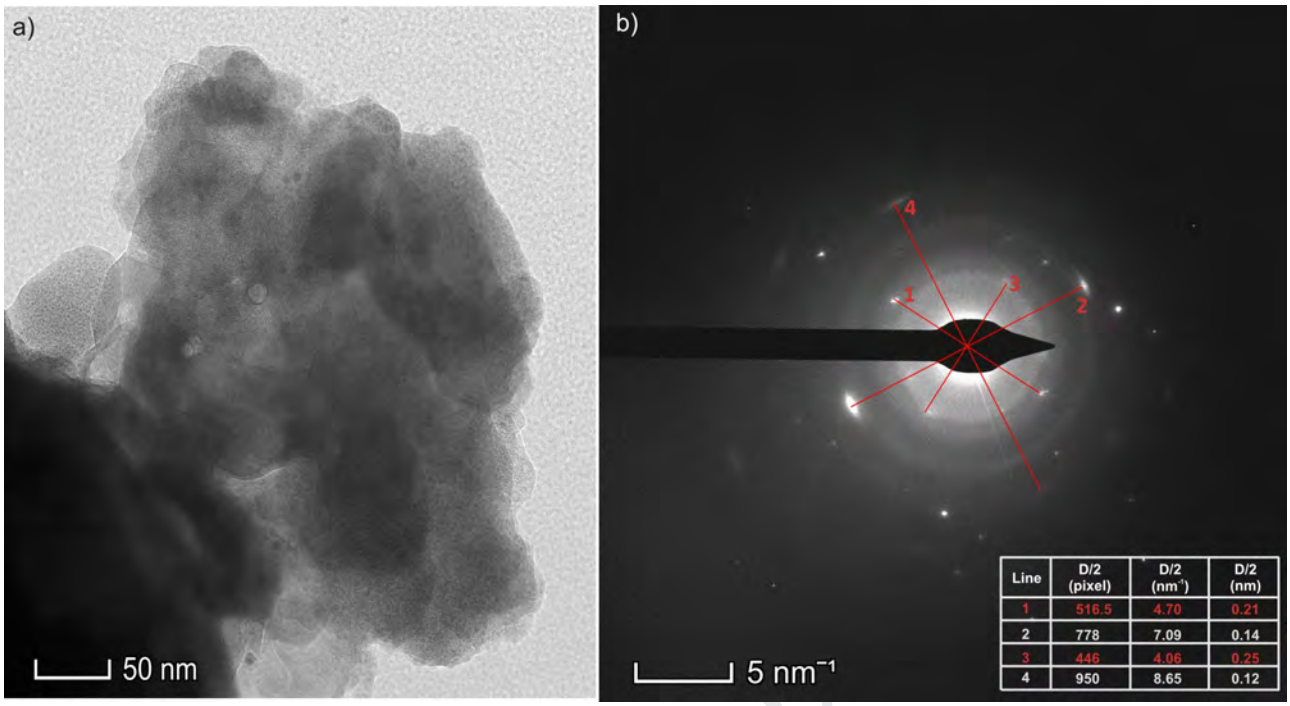

Figure 8

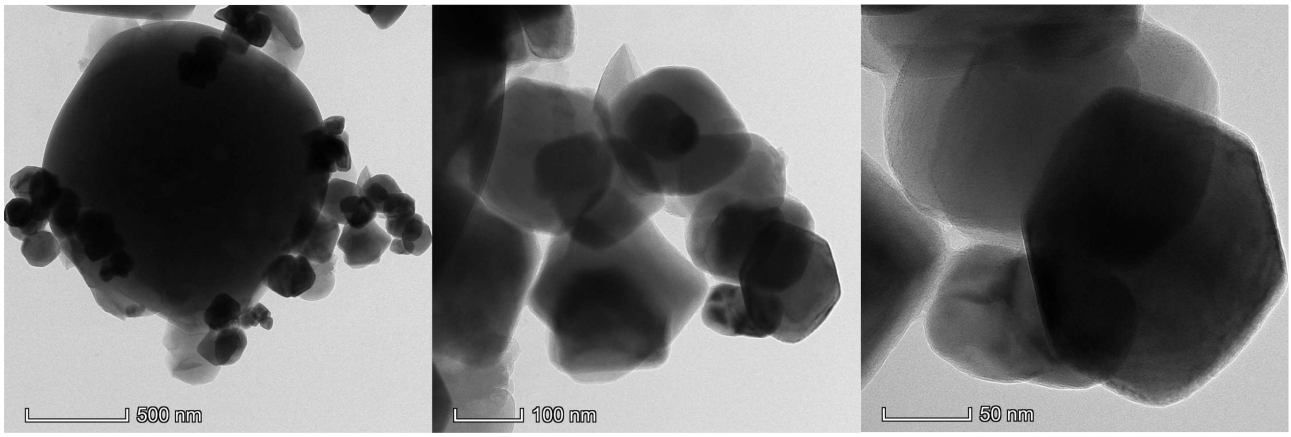

Figure 9

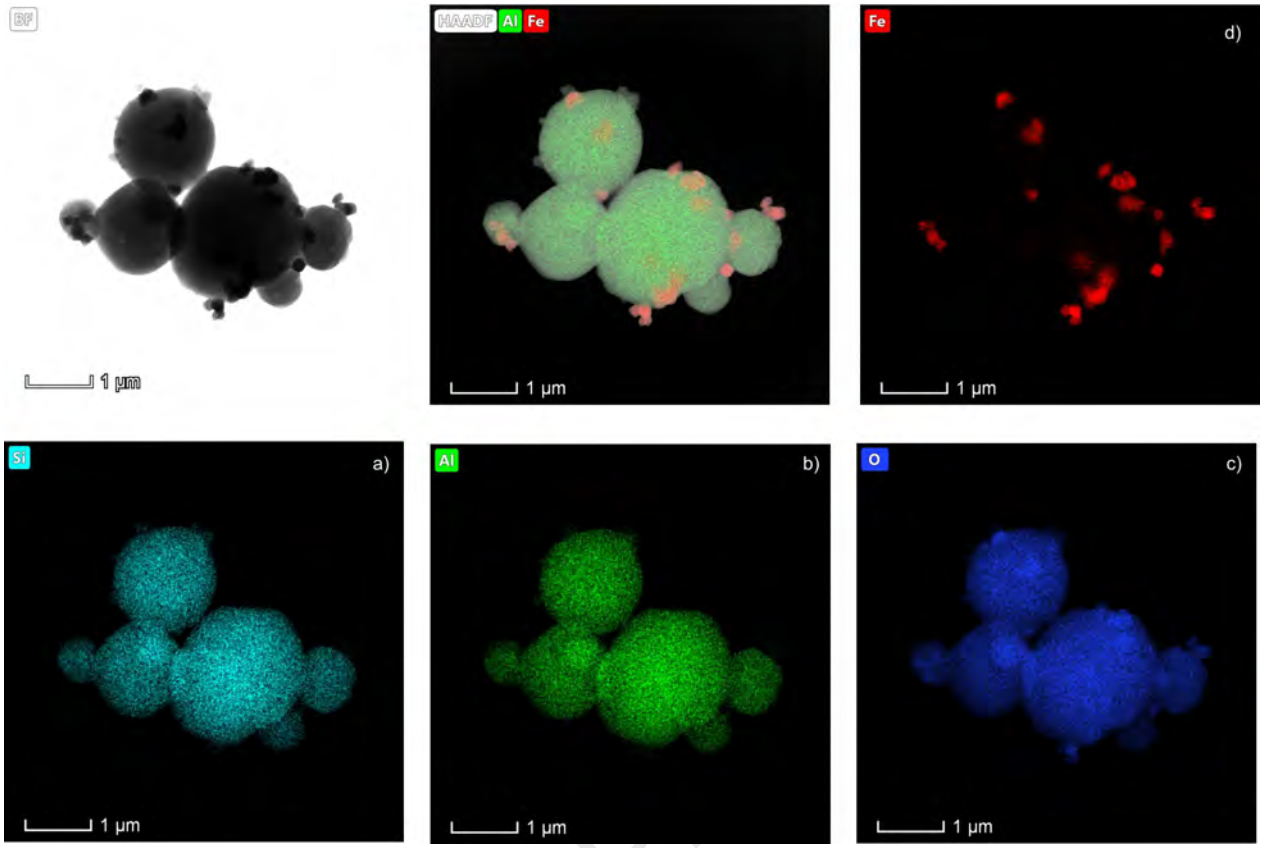

Figure 10

Table 1. XRF chemical composition of Red mud (wt%).

	Zn	Pb	Cu	FeO	CaO	Al_2O_3	MgO	Cd	Ag	Mo	SiO_2	H_2O	S tot
Red mud	6.76	3.61	0.14	37.04	1.09	0.89	0.31	0.08	137	61	4.23	33.78	9.26

Table 2. Synthetic products (wt%) based on Rietveld full-profile fit of the X-ray diffraction data (uncertainty: +/- 1 wt%).

Samples	LTA zeolite	Franklinite	Hematite
S3	98.0	2.0	
S5	91.4	8.6	
S6	93.1	6.9	
S10	83.3		16.7
S11	83.6		16.4

Captions Supporting Materials

Figure S1.
SEM images of pure LTA.

Figure S2.
SEM images of LTA zeolite formed by a 4-day conventional hydrothermal synthesis.

Figure S3.
SEM image of LTA zeolite formed by a 4-day pre-fused hydrothermal process.

Figure S4.
TEM images of LTA zeolite formed by conventional hydrothermal synthesis.

Figure S5.
TEM images of LTA zeolite formed by pre-fused hydrothermal process.

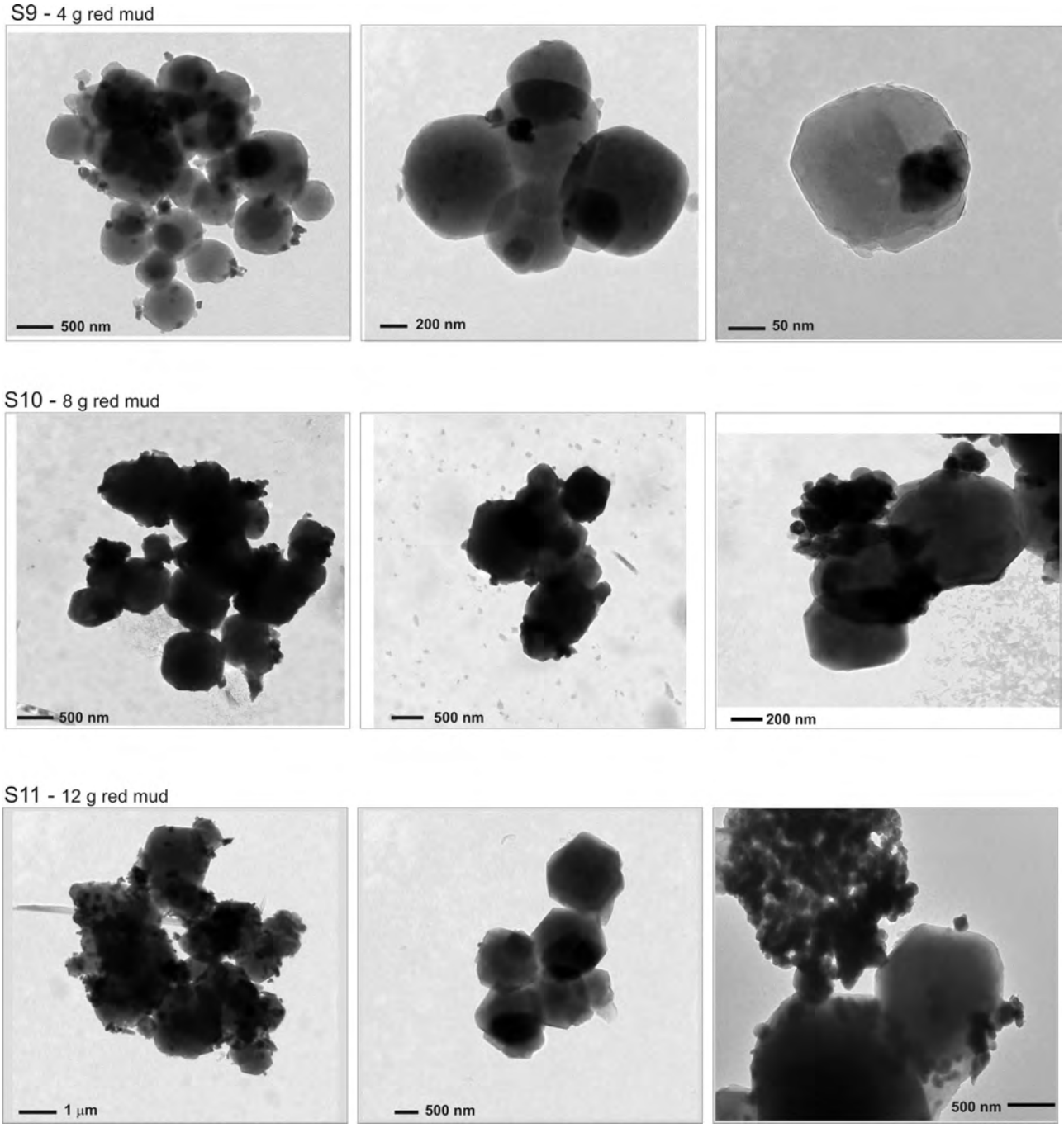
S9 - 4 g red mud
500 nm
200 nm
50 nm
S10 - 8 g red mud
500 nm
500 nm
200 nm
S11 - 12 g red mud
1 μm
500 nm
500 nm

S1

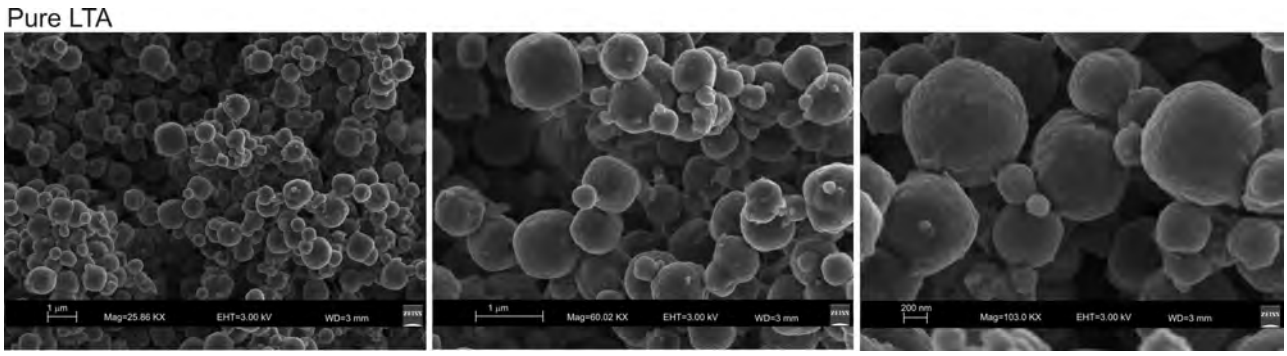

S2

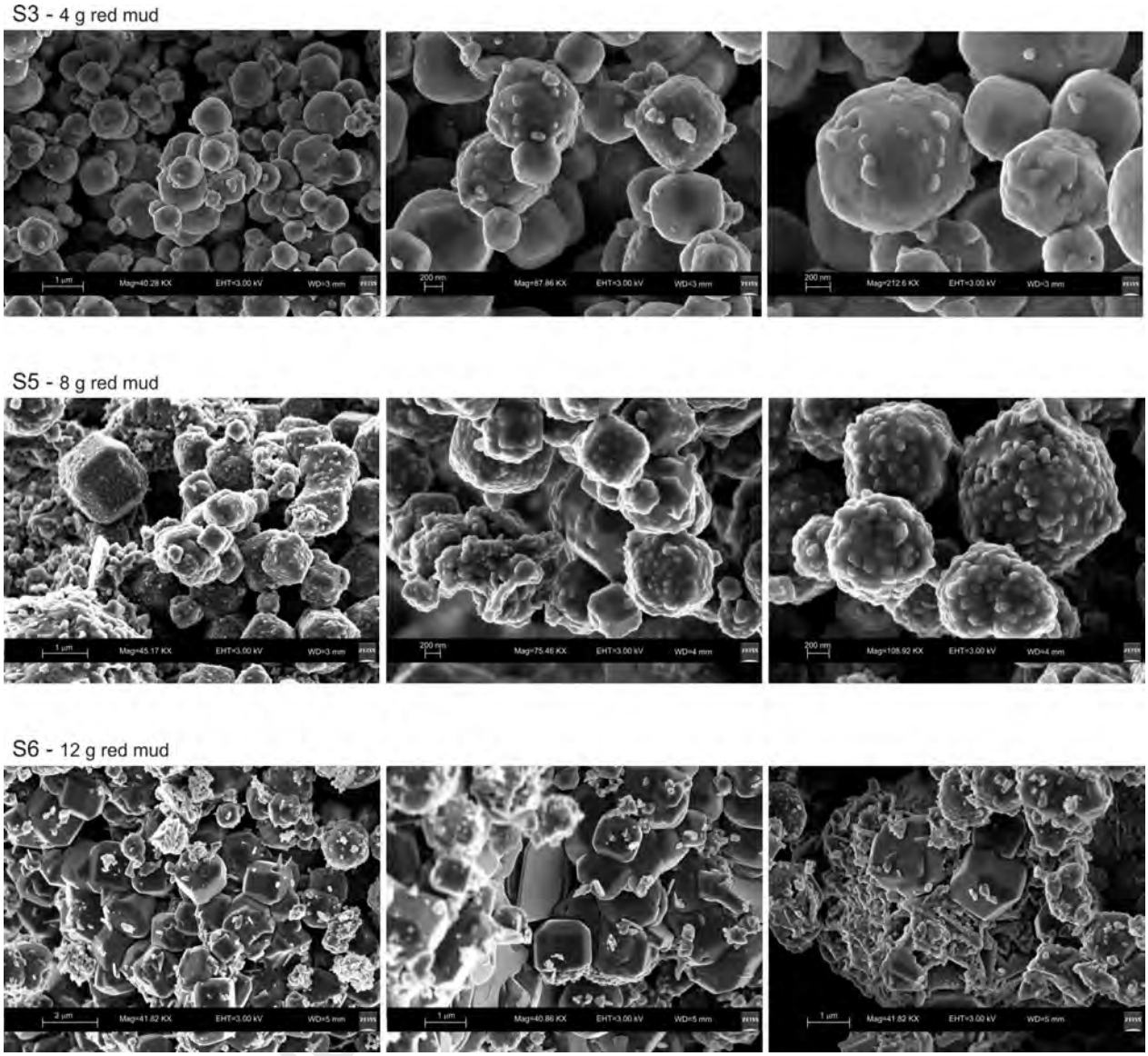

S3

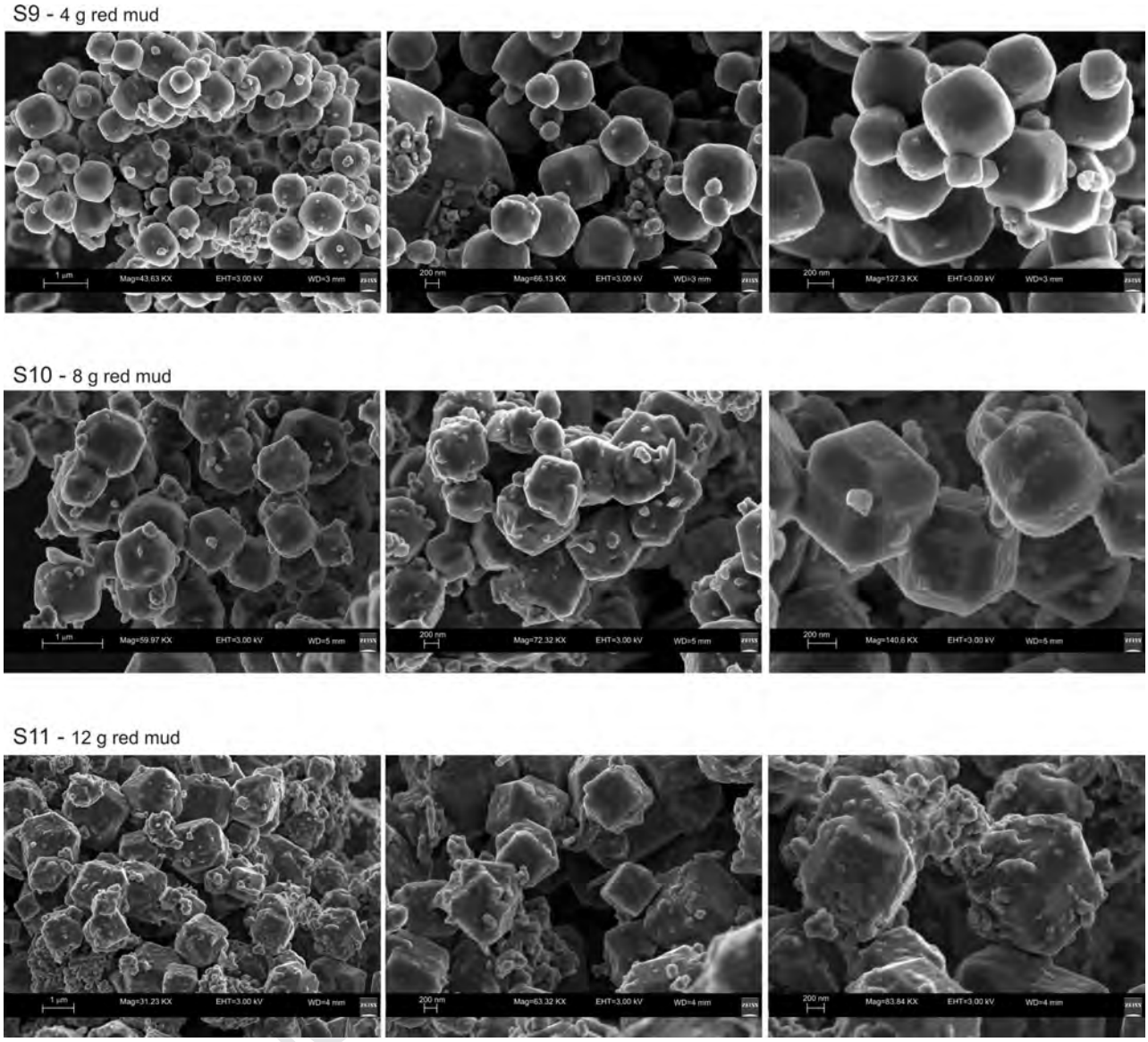

S4

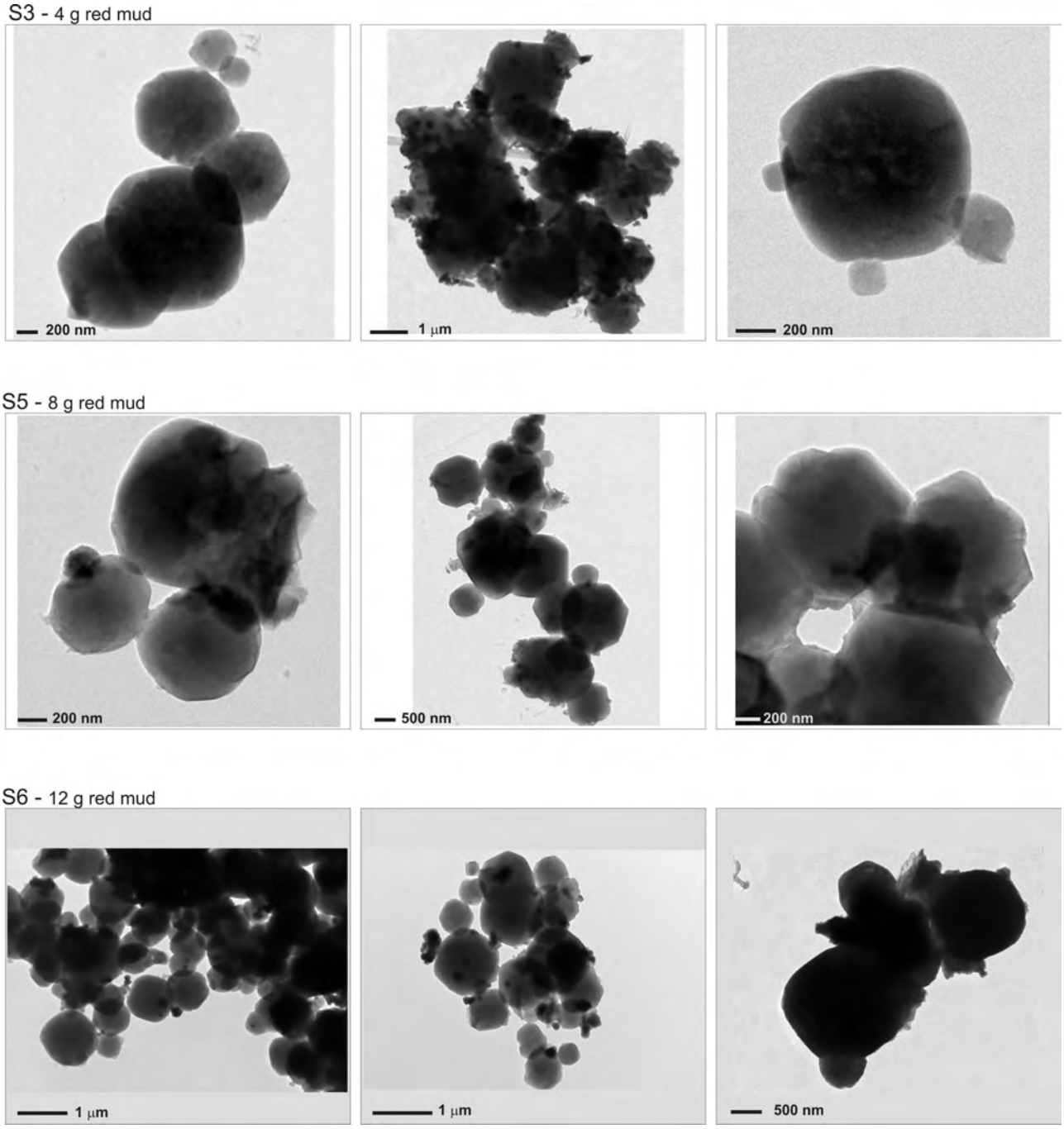
S3 - 4 g red mud
200 nm
1 μm
200 nm
S5 - 8 g red mud
200 nm
500 nm
200 nm
S6 - 12 g red mud
1 μm
1 μm
500 nm

S5

Table S1. Unit-cell edge of the LTA zeolites
(uncertancy +/- 0.0005 A on unit-cell edge leght, +/- 0.5 A3 on the volume)

Samples	*a* (Å)	*V*(Å^3)
pure LTA	24.5618	14817.7
S3	24.5549	14805.3
S5	24.5401	14778.0
S6	24.5338	14767.0
S10	24.5702	14832.0
S11	24.5667	14826.0

Table 1. XRF chemical composition of Red mud (wt%).

	Zn	**Pb**	**Cu**	**FeO**	**CaO**	**Al_2O_3**	**MgO**	**Cd**	**Ag**	**Mo**	**SiO_2**	**H_2O**	**S tot**
Red mud	6.76	3.61	0.14	37.04	1.09	0.89	0.31	0.08	137	61	4.23	33.78	9.26

Table 2. Synthetic products (wt%) based on Rietveld full-profile fit of the X-ray diffraction data (uncertainty: +/- 1 wt%).

Samples	LTA zeolite	Franklinite	Hematite
S3	98.0	2.0	
S5	91.4	8.6	
S6	93.1	6.9	
S10	83.3		16.7
S11	83.6		16.4

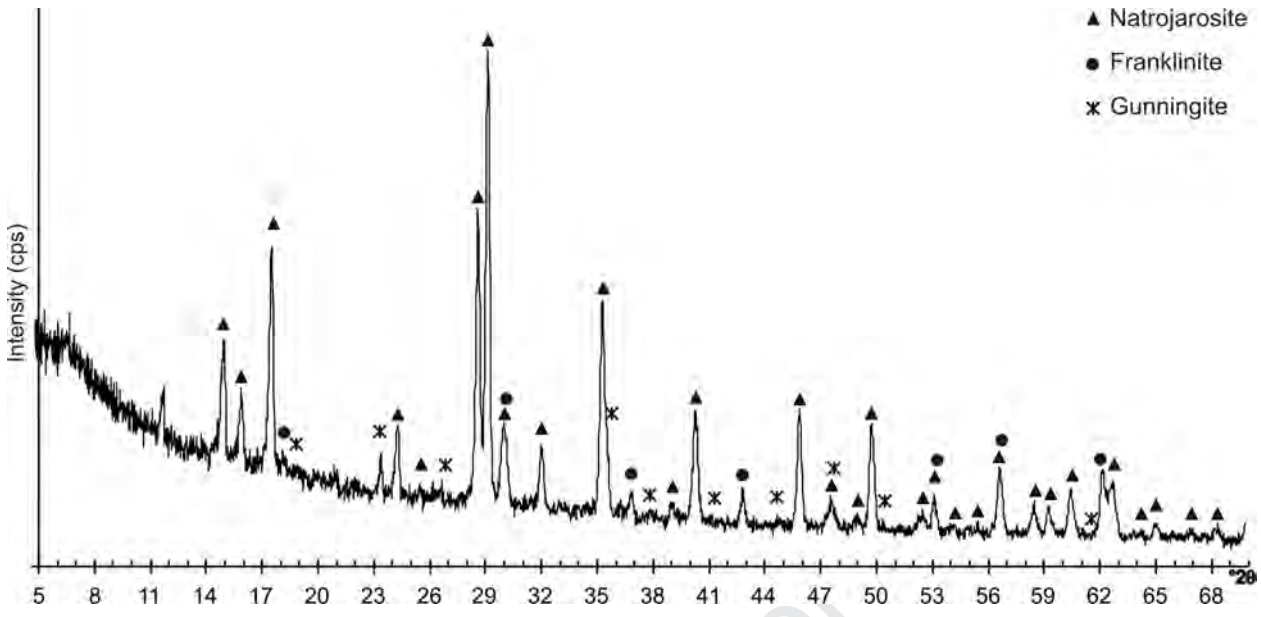

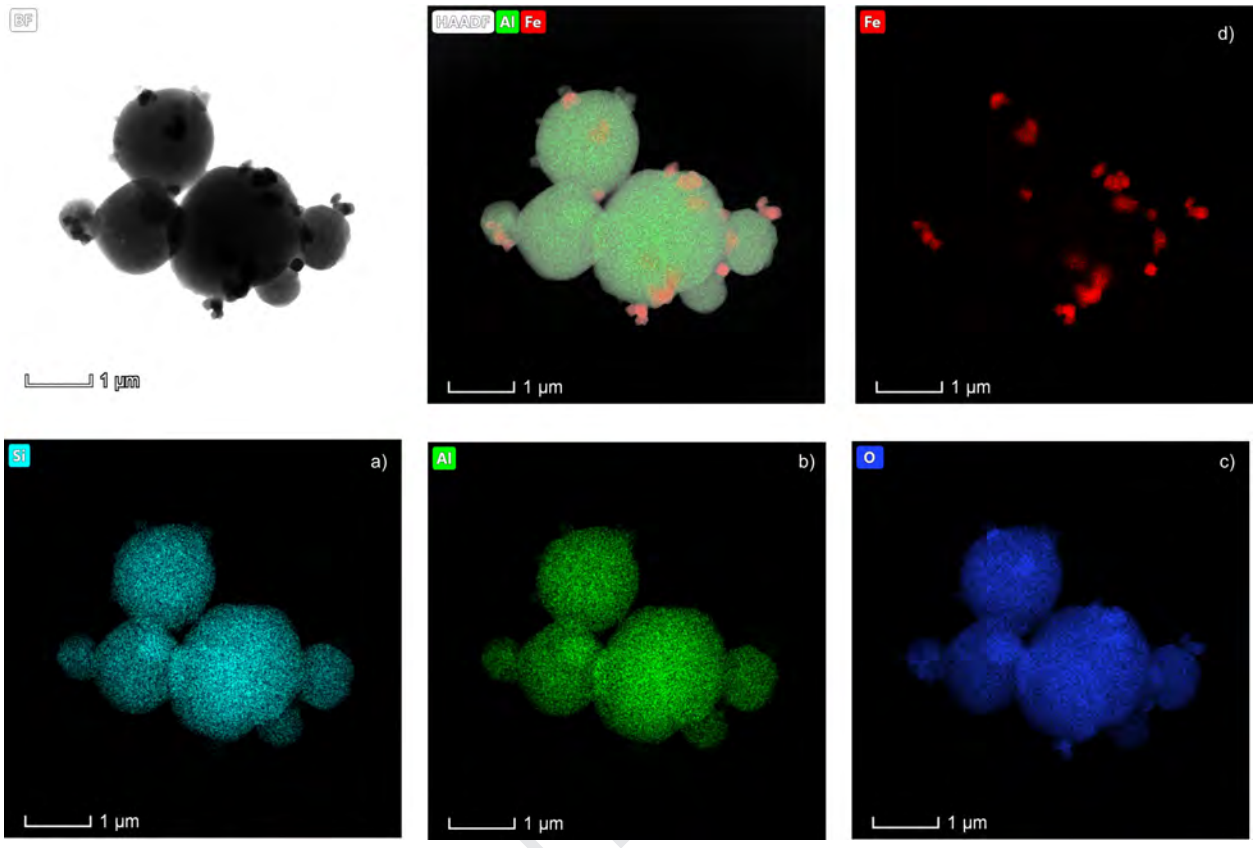

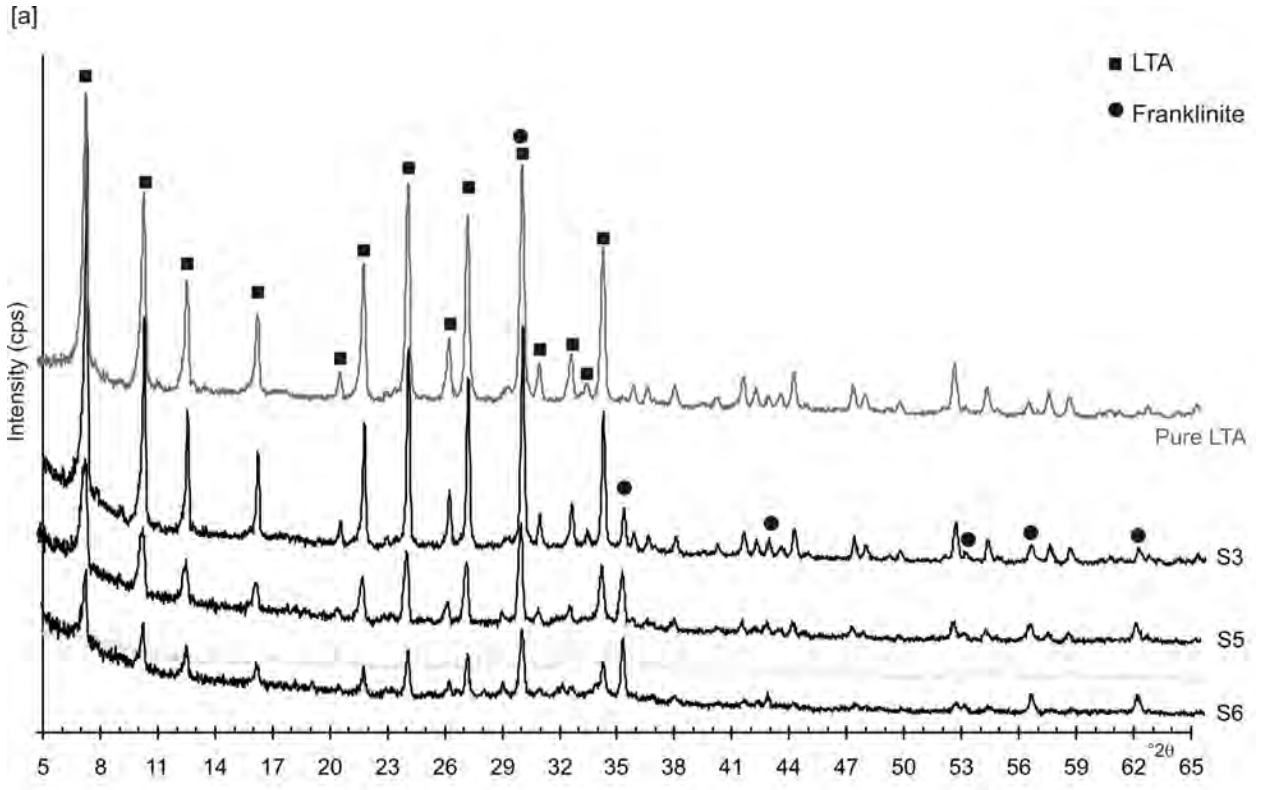
[a]
LTA
Franklinite
Intensity (cps)
Pure LTA
S3
S5
S6
5 8 11 14 17 20 23 26 29 32 35 38 41 44 47 50 53 56 59 62 65
°2θ

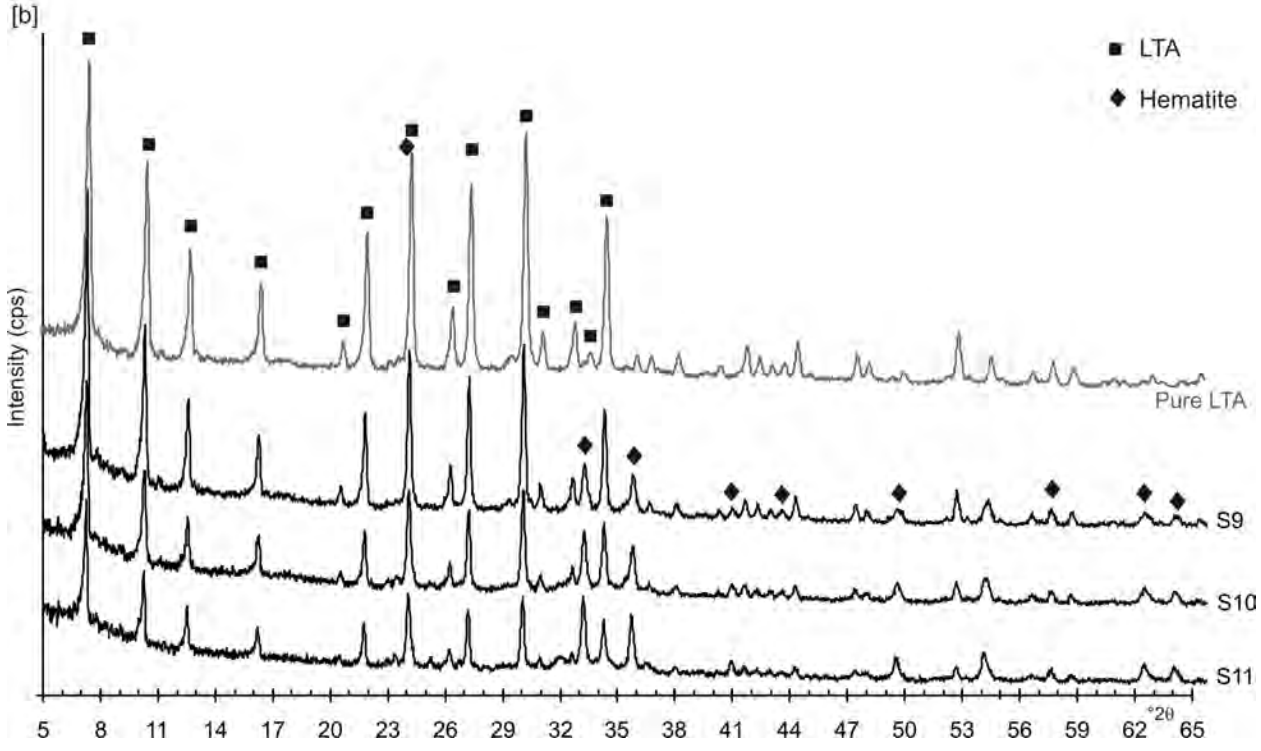
[b]
LTA
Hematite
Intensity (cps)
Pure LTA
S9
S10
S11
5 8 11 14 17 20 23 26 29 32 35 38 41 44 47 50 53 56 59 62 65
°2θ

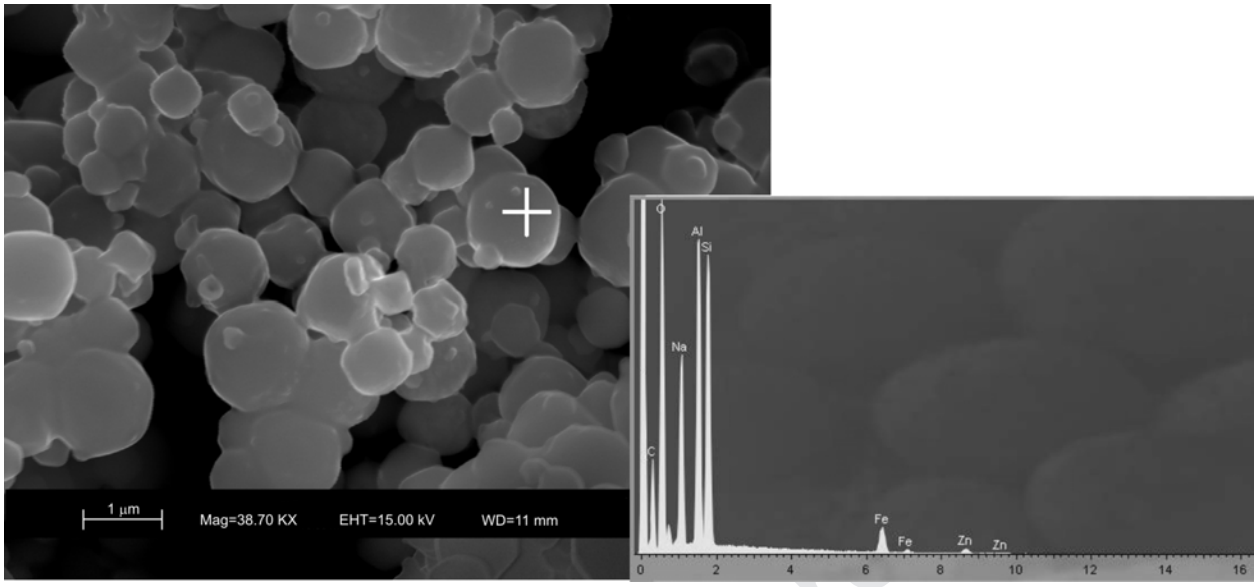

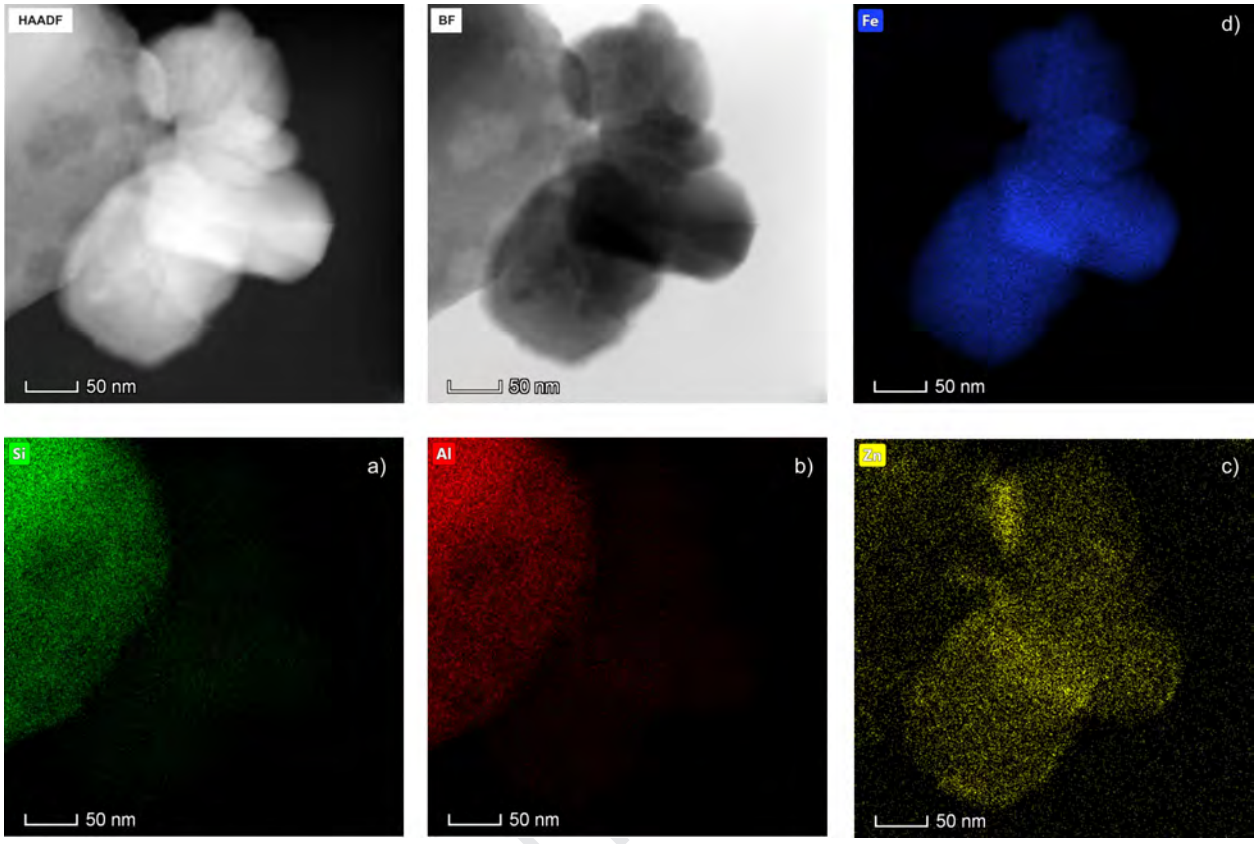

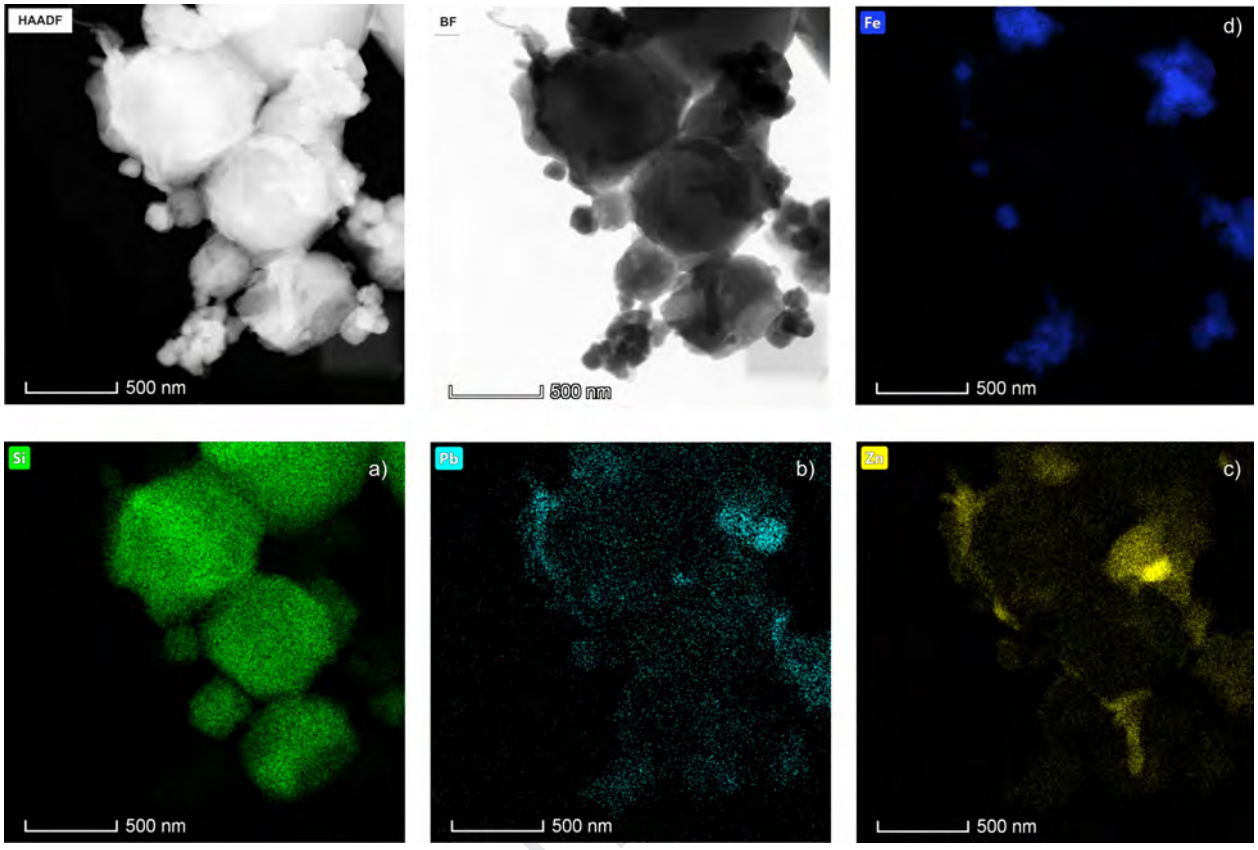

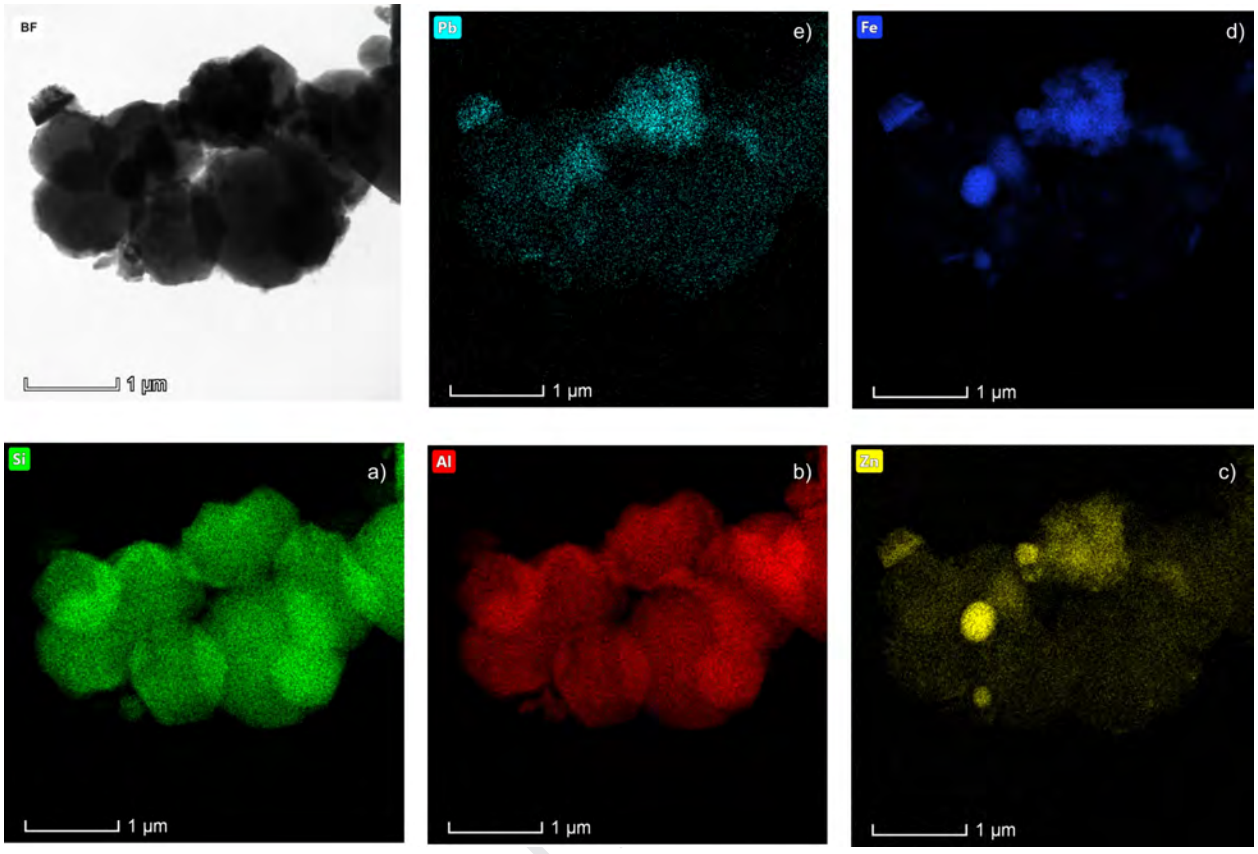

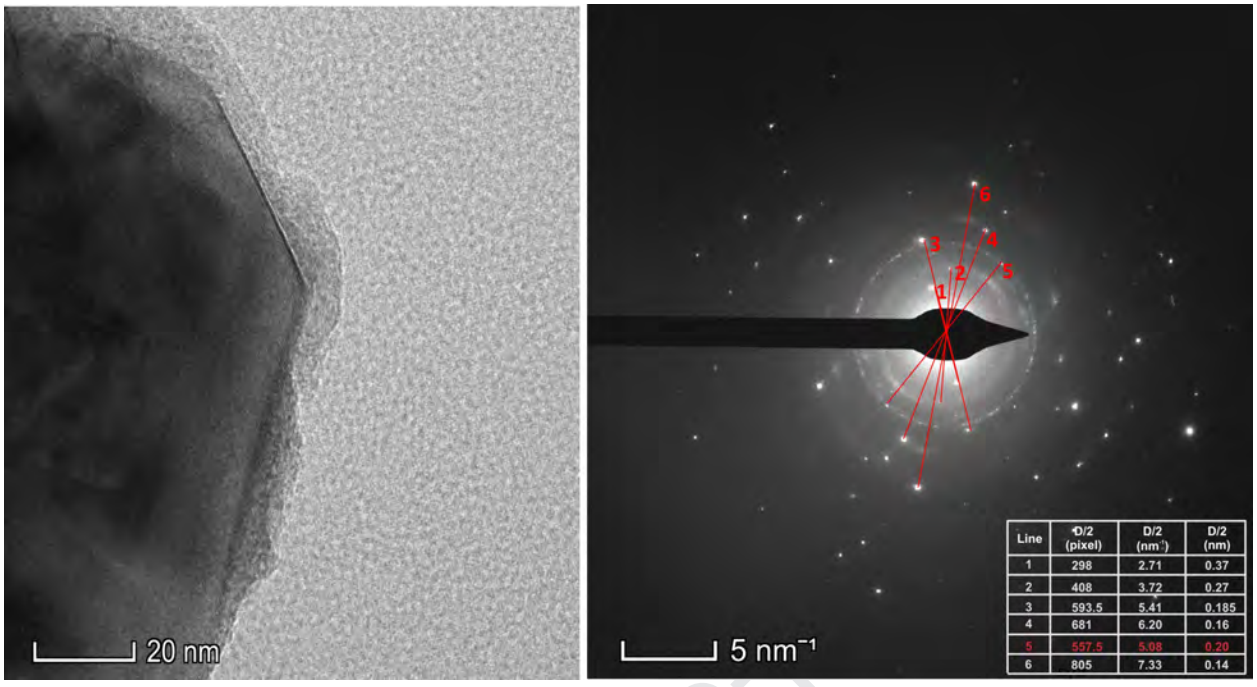

Line	D/2 (pixel)	D/2 (nm⁻¹)	D/2 (nm)
1	298	2.71	0.37
2	408	3.72	0.27
3	593.5	5.41	0.185
4	681	6.20	0.16
5	557.5	5.08	0.20
6	805	7.33	0.14

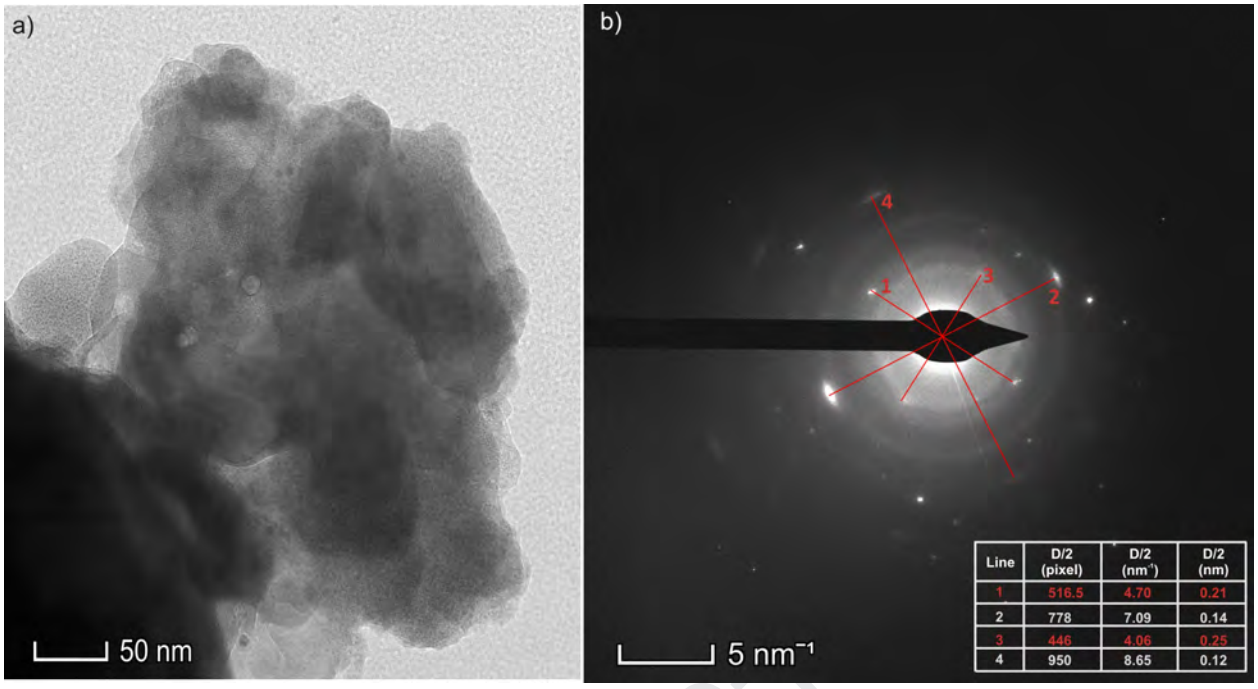

Line	D/2 (pixel)	D/2 (nm^{-1})	D/2 (nm)
1	516.5	4.70	0.21
2	778	7.09	0.14
3	446	4.06	0.25
4	950	8.65	0.12

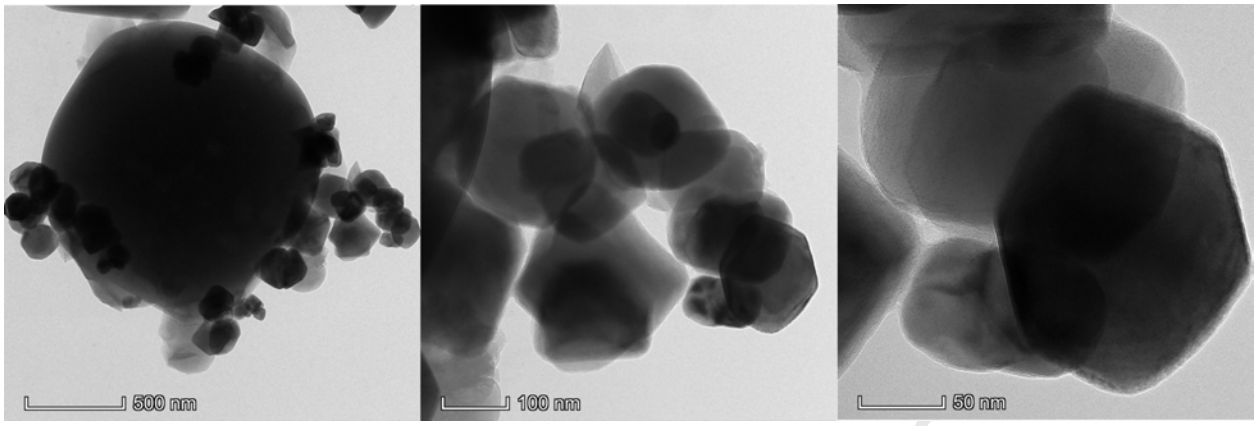

Highlights

- Material: LTA zeolite formed using pure sources combined with red mud;
- Red mud: a waste formed during the bauxite caustic leaching to produce alumina;
- Aim: mobilize Fe coming from red mud within the newly formed zeolite structure;
- Results: Fe concentrated in nano-clusters on the zeolite crystal surface;
- Techniques: XRPD, SEM-EDX, synchrotron radiation XRD, TEM-EDX elemental mapping

C.B. and G.D.G. led the structure search. All Authors contributed to the discussion and writing of the manuscript.

Captions

Figure 1.
XRPD patterns of the red mud used in this study.

Figure 2.
XRPD profiles of synthesis products by: [a] conventional hydrothermal process [b] pre-fused hydrothermal process

Figure 3.
EDX spectrum representative of the LTA zeolite crystals formed by adding RM during the synthesis

Figure 4.
TEM images (left-up) and relative EDX elemental mapping of : *a*) Si, *b*) Al, *c*) Zn and *d*) Fe. S5 sample.

Figure 5.
TEM images (left-up) and EDX elemental mapping of : *a*) Si, *b*) Al, *c*) Zn, *d*) Fe and *e*) Pb. S5 sample.

Figure 6.
TEM images (left-up) and EDX elemental mapping of Si, Al, Zn, Fe and Pb elements (*a*-*e*). S10 sample.

Figure 7.
S5 sample. *a*) high-resolution image of a zeolite crystal and irregular aggregates of nano-sized particles lying on its surface; *b*) electron diffraction pattern showing single spots ascribable to the zeolite crystal and diffraction rings generated by the Fe-Zn-bearing nano-clusters (highly likely with spinel-type structure). A table with the geometric parameters is provided.

Figure 8.
S10 sample. *a*) high-resolution images of zeolite crystals and irregular aggregates of nano-sized particles; *b*) co-existing electron diffraction patterns of a zeolite crystal and Fe-Zn bearing nano-clusters (with a table of their geometric parameters).

Figure 9.
TEM images of the SnM zeolite formed by conventional hydrothermal synthesis with nano-magnetite.

Figure 10.
TEM images (left-up) and EDX elemental mapping of : *a*) Si, *b*) Al, *c*) O and *d*) Fe. SnM sample.

The authors declare no competing financial interest.